UTRECHT UNIVERSITY

MASTER THESIS

Phase slips in space-time crystals

Author:
Bsc. Jillis Bernard Eduard Schokking

Daily Supervisor:
Nejc Blaznik MSc.
First Supervisor:
Prof. Dr. Peter van der Straten
Second Supervisor:
Prof. Dr. Ir. Henk Stoof

This research was conducted in

Nanophotonics Group of the Debye Institute
Master Program Experimental Physics

November 17, 2022

Front image modified from the July 2018 issue of Physics World

UTRECHT UNIVERSITY

Abstract

Debye Institute
Master Program Experimental Physics

master's degree in Physics

Phase slips in space-time crystals

by Bsc. Jillis Bernard Eduard Schokking

Time crystals are a novel phase of matter in physics. In this work we focus on one particular realization, an axial density oscillation in a Bose-Einstein condensate of Sodium atoms. Expanding on a previously developed quantum mechanical description of the time crystal, our goal is to explore the parameter space in which dynamics between crystal modes can arise and characterise this behaviour. In order to study the large parameter space of our system, fast approximate models are desirable. We employ three models to study switching between time crystal modes. The first is a one dimensional toy model, the second quantum trajectory calculations based on the Langevin equations of motion, and third a two dimensional numerical evaluation of the Fokker-Planck equation. The one dimensional model fails near the origin of the phase space describing the time crystal, preventing mode interaction. The quantum trajectory approach is shown to agree qualitatively with evaluation of the Fokker-Planck equation, both predicting over and under-damped probability oscillations between crystal modes.

Contents

List of Figures

Chapter 1

Introduction

From ancient Greek philosophers to the steam engine powering the industrial revolution, the investigation of the phases in which matter can occur goes back centuries. Where once the ability of water to form solid, liquid and a gaseous phase was a mystery, our present day understanding of matter does not only allow for a full description of these phenomena, but also led to new kinds of exotic phases of matter. The extremely energetic quark-gluon plasma in the Large Hadron Collider for example, or liquid crystals in our everyday displays. And at very low temperatures, the Bose-Einstein condensate (BEC).

1.1 History of the Bose-Einstein Condensate

The start of the 20th century heralded one of the most important breakthroughs in physics, Quantum Mechanics. Planck's law describing black body radiation, published in 1900 [1], predicted light to consist of discrete packets of energy. This contradicted the physical framework of the time. The Indian physicist Satyendra Nath Bose succeeded in developing a quantum theory around this phenomenon, but had difficulty getting his controversial work published. He reached out to Albert Einstein with an offer to collaborate, which was successful[2]. Einstein extended his theory to include particles with mass, deriving the full thermodynamic relations in 1925 [3]. This theory made a remarkable prediction, the number of thermal (bosonic) particles in a closed system has an upper bound which decreases with lower temperatures. When there are more particles than thermal states available, the excess particles start to occupy the same lowest energy state. This new state of matter is called the Bose-Einstein condensate.

The first experimental realization of the BEC was in 1932 using Helium-4, which required a temperature in the order of 2 K [4]. These were high density condensates and are hard to describe theoretically, but do exhibit super-fluidity. Lower density condensates require temperatures in the order of nano-Kelvins, which was impossible with the technology of that time. It took 70 years of advancement until the first experimental observation of a gaseous BEC. In 1995 the group by Cornell and Wieman at NIST-JILA realized the first Bose-Einstein condensate using Rubidium atoms [5]. In the same year, the group of Wolfgang Ketterle at MIT succeeded using sodium atoms [6]. Both groups were awarded the Nobel prize in 2001. In Utrecht the first BEC was created in 2004 using stable Sodium atoms [7]. The BEC is essentially a matter wave, which can create interference patterns. These were investigated by Alexander de Groot and later by J. Smits [8], [9]. Among other findings, an oscillating density mode was discovered in an anisotropic cigar-shaped trap. Driven by a periodic stretching in the width of the condensate, a so-called breathing mode, a higher order axial oscillation is excited. This axial mode breaks the symmetry of its driving mechanism. A time crystal.

1.2 Broken Symmetry

Symmetries play a fundamental role in physics. Emmy Noether showed in her famous theorem that for every continuous symmetry of a system there is a conservation law, and vice versa [10]. A second fundamental connection with symmetries occurs in the study of phase transitions. Water at room temperature is fluid, at a microscopic level one can translate or rotate it at will, and it will look the same. Water therefor has continuous translation and rotational symmetry. Below the freezing point, it undergoes a phase transition to a solid phase; ice. The atoms are arranged in a periodic structure, which has a discrete translation and rotational symmetry. Phase transitions break or reduce symmetries of the system. Another example, when a magnetic material is cooled below the Curie temperature, spatial isotropy is broken when the magnetic moments of the constituent particles collectively align.

In physics, a system is described though a Hamiltonian. This formulation too possesses symmetry. In analogy with the breaking of a spatial symmetry, in 2012 Frank Wilczek [11] proposed a system that in the ground state it breaks continuous time translation symmetry of the governing Hamiltonian. Met with criticism, this idea started a discussion that is still ongoing today. In 2015 Watanabe showed that a system in equilibrium cannot break continuous time symmetry, a no-go theorem for time crystals[12]. This left some loopholes for continuous time crystals, such as considering higher energy states, long range order or dissipate systems [13]–[15]. Breaking discrete time symmetry in a periodically driven, out of equilibrium system is another workaround. This is where the current focus in the search of time crystals lies.

1.3 Discrete Time Crystals

In the last few years a number of time crystals that break discrete time symmetry have been discovered. Among others, in nitrogen–vacancy impurities in diamond and trapped ion chains[16], [17]. These are examples of Floquet systems, where the governing Hamiltonian has a period T. Upon measurement, this symmetry is broken spontaneously. The resulting dynamics have a period $n \times T$, an integer multiple. As a consequence, multiple modes that differ in a phase offset with respect to the drive are possible. Upon excitation, the system picks one of the solutions. Recent work suggested not only that it is possible to switch between crystal modes[18], but also succeeded experimentally in a dissipative atom-cavity system[19]. The focus of this thesis is to explore mode switching in time crystals. In contrast to previous research, here the description of the time crystal itself is quantum mechanical, based on the work by Stehouwer[20]. From this standpoint, switching between modes is analogous to quantum tunneling. Or when in a coherent fashion, to Rabi oscillation.

1.4 Thesis Outline

This work is setup as follows. In chapter 2 the dynamics of the condensate are discussed and derives a quantum mechanical description of the time crystal. Chapter 3 presents the numerical algorithms used to study the equations in chapter 2. The results of these simulations are presented in Chapter 4. An overview of the experimental setup is given in chapter 5. Chapter 6 discusses the achieved results and provides conclusions and outlook.

Chapter 2

Theory

2.1 The Bose Einstein Condensate

The following theoretical discussion is based on the book *Bose–Einstein Condensation in Dilute Gases* by Pethick and Smith [21]. When a cloud of bosonic particles is sufficiently cooled, a significant fraction will start to occupy the ground state. This low energy state of matter is called a Bose-Einstein condensate. Bose-Einstein Condensation occurs when the inter-particle distance becomes comparable with the thermal wavelength,

$$\lambda_{db} = \sqrt{\frac{2\pi\hbar^2}{mK_bT}}. \tag{2.1}$$

At high temperature particles in the cloud are distributed over energy states according to Bose statistics, with a weight $\frac{1}{e^{\epsilon/K_bT}-1}$. As the cloud cools down fewer energy states become available. Because bosons can occupy the same state, at a critical temperature $T = T_c$ particles will start to occupy the lowest energy state, as illustrated by 2.1. For low density condensates like the ones created in Utrecht, this happens usually in the order of nano Kelvins. Particles in this low energy state are the Bose-Einstein condensate. Any particles remaining in higher energy states are referred to as the thermal cloud.
A common choice for the trapping potential is the anisotropic harmonic trap. For particles with mass m,

$$V(\rho, z) = \frac{1}{2}m\omega_\rho^2(\rho^2 + \lambda^2 z^2). \tag{2.2}$$

The trapping frequency in the axial z direction and radial ρ direction are related by a scale factor $\omega_z = \lambda\omega_\rho$, with $\lambda < 1$ resulting in a cigar-shaped trap. When in equilibrium, the wavefunction of the condensate is described by the time-independent Gross–Pitaevskii equation,

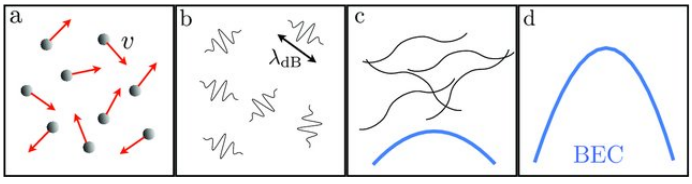

FIGURE 2.1: Illustration of particles at different temperatures. At high temperature particles are classical. As the temperature decreases from left to right, the thermal wavelength increases. When this becomes comparable with the inter-particle distance, the BEC forms. Image taken from Corgier [22].

$$\mu\psi(\mathrm{r}) = -\frac{\hbar^2}{2m}\nabla^2\psi(\mathrm{r}) + V(\mathrm{r})\psi(\mathrm{r}) + U_0|\psi(\mathrm{r})|^2\psi(\mathrm{r}). \tag{2.3}$$

This is a nonlineair Schrödinger equation, with a two-body interaction term $U_0 = 4\pi\hbar^2 a_s/m$ and chemical potential μ. It depends on the s-wave scattering length a_s. This is justified because at low energies the effective interaction between two particles is constant. From here, the equilibrium distribution can be derived. For this we will assume that the kinetic energy of the particles in BEC is negligible compared to the trapping potential. This is called the Thomas-Fermi limit, which holds true except at the surface of the condensate.

$$\mu\psi(\mathrm{r}) = V(\mathrm{r})\psi(\mathrm{r}) + U_0|\psi(\mathrm{r})|^2\psi(\mathrm{r}). \tag{2.4}$$

We can solve this for the density distribution $n(\mathrm{r})$, which follows the parabolic shape of the trap,

$$n(\mathrm{r}) = |\psi(\mathrm{r},t)|^2 = \frac{\mu - V(\mathrm{r})}{U_0}. \tag{2.5}$$

The boundary of the condensate is given by $V(\mathrm{r}) = \mu$. This yields a way to measure the chemical potential by determining the boundary of the condensate during experiment. The phenomena we are interested in happen outside of equilibrium however, for which we use the time-dependent Gross–Pitaevskii equation,

$$i\hbar\frac{\partial\psi(\mathrm{r},t)}{\partial t} = -\frac{\hbar^2}{2m}\nabla^2\psi(\mathrm{r},t) + V(\mathrm{r})\psi(\mathrm{r},t) + U_0|\psi(\mathrm{r},t)|^2\psi(\mathrm{r},t). \tag{2.6}$$

One interesting aspect of BEC is that it exhibits superfluidity. We can reformulate this equation in terms of density n and phase ϕ, $\psi = \sqrt{n}e^{i\phi}$. After substitution in equation 2.6 and separating the real and imaginary parts, one finds a continuity equation for the density as well as an important relation for the phase. Both relations will be derived in the next section through Lagrangian formalism, which is equivalent to the fluid description. Upon introducing excitations to the system, a number of collective modes emerge, illustrated in figure 2.2. One may refer to *Bose–Einstein Condensation in Dilute Gases* for a detailed derivation, here we will focus on the two modes that play a role in the creation of spacetime crystals, the breathing mode and axial modes.

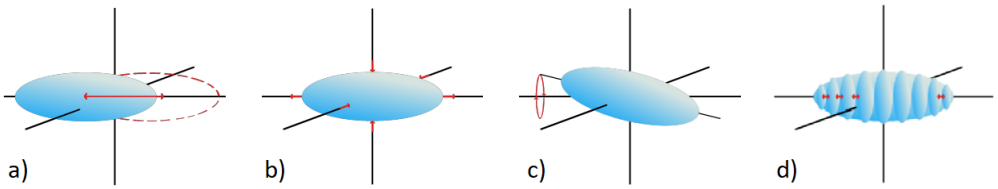

FIGURE 2.2: Illustration of different modes of the BEC in an anisotropic trap. a) The axial dipole mode, the centre of mass oscillates in the axial direction. b) The breathing mode, the BEC stretches and contracts with a different frequency in the radial and axial direction. c) The Scissor mode, the condensate precesses around the axial dimension. d) Higher order axial mode, where the density oscillates only in the the axial direction. Image modified from *Crystallized time in ultra-cold Bose gases* by S. Borman[23].

The breathing mode stretches the condensate, equivalent to adding a scale factor to the dimesions of the condensate. It oscillates at a frequency

$$\omega^2 = \omega_\rho^2(2 + \frac{3}{2}\lambda^2 \pm \frac{1}{2}\sqrt{16 - 16\lambda^2 + 9\lambda^4}). \tag{2.7}$$

The positive root corresponds with the radial breathing mode, the negative with the axial breathing mode. The frequency of the breathing mode depends on that of the trap. Crucially, the radial component of this mode couples to higher order axial modes which we will discuss in the next section.

2.2 Higher order axial mode

In this section we will derive the higher order axial mode and how it relates to time-crystals. It will follow the paper *Dynamics of a Space-Time Crystal in an Atomic Bose-Einstein Condensate* by Liao et al.[24]. The condensate is fully described by the density $n(\mathrm{r}, t)$ and phase $\phi(\mathrm{r}, t)$. The effective action of this system is given by

$$S = \int \mathrm{d}t \int \mathrm{d}\mathbf{r}\, L, \tag{2.8}$$

with the Lagranian density

$$L = -\hbar n \frac{\partial \phi}{\partial t} - nV(\mathrm{r}) - \frac{U_0}{2}n^2 - \frac{\hbar^2}{2m}\big[\frac{(\nabla n)^2}{4n} + n(\nabla\phi)^2\big]. \tag{2.9}$$

Minimizing the action $\delta S/\delta\phi = 0$ yields a continuity equation for the density,

$$\frac{\partial n}{\partial t} = -\nabla \cdot (n(\mathrm{r}, t)\frac{\hbar\nabla\phi(\mathrm{r}, t)}{m}). \tag{2.10}$$

When interpreted as a continuity equation of a friction-less (ideal) fluid, we can identify in the right lid a flow velocity $\mathrm{v} = \hbar\nabla\phi(\mathrm{r}, t)/m$. Because ϕ is a scalar quantity, we know $\nabla \times \mathbf{v} = 0$. This already lays a restriction the motion of the condensate. Similarly, by minimizing the action with respect to the density, $\delta S/\delta n = 0$, we find

$$\hbar\frac{\partial\phi}{\partial t} + (\frac{1}{2}m\mathrm{v}^2 + V + U_0 n\frac{\hbar^2}{2m\sqrt{n}}\nabla^2\sqrt{n}) = 0. \tag{2.11}$$

It can be shown that the phase develops in time as $\dot{\phi} = -\frac{\mu}{\hbar} = -\frac{\delta E}{\hbar\delta N}$. This is the Josephson relation, which links the energy required to add a particle to the system to the overall phase. Equation 2.11 is therefor referred to as the Josephson equation. In the Thomas-Fermi limit we neglect the kinetic contribution in the GP equation, in this Lagrangian formalism this is equivalent to ignoring the quantum pressure term in equation 2.9, the term proportional to ∇n^2. We assume density modulation to be small, such that we may split density and phase a radial and axial part, $n = n_D + n_A$ and $\phi = \phi_N + \phi_A$. Considering only the second-order and third-order terms of n_A and ϕ_A in equation 2.9, the Lagrangian density governing the axial mode reduces to

$$L_a = -\hbar n_A\frac{\partial\phi_A}{\partial t} - \frac{U_0}{2}n_a^2 - \frac{\hbar}{2m}\big[n_D(\nabla\phi_A)^2 + 2n_A\nabla\phi_D\cdot\nabla\phi_A + n_A(\nabla\phi_A)^2\big]. \tag{2.12}$$

Radial mode excitations are more energetic compared to the axial mode, so we can expect coupling to many higher order axial modes. We then write the total number of excitations as a sum over all modes, indexed with the quantum mode number j,

$$n_A = \sum_j n_j \quad \phi_a = \sum_j \phi_j. \tag{2.13}$$

Next we wish to expand this in a set of basis functions. In one dimension with a harmonic trapping potential, Legendre polynomials $P_j(\tilde{z})$ on scaled coordinate $\tilde{z} = z/R_z$ provide an exact solution. Here R_z is the size of the condensate. Experimental observations show little too no radial dependence[25], making Legendre polynomials good candidates. These must satisfy the boundary conditions of the condensate, i.e. the density should go to zero. Therefor we take the difference

$$L_j(\tilde{z}) = P_{j+2}(\tilde{z}) - P_j(\tilde{z}) \tag{2.14}$$

as basis, to ensure decay at the edges. We then take the variational anzatz

$$n_j(z,t) = -\dot{\kappa_j}(t) L_j(\tilde{z}), \tag{2.15}$$

$$\phi_j(z,t) = \frac{U_0}{\hbar} \kappa_j(t) L_j(\tilde{z}). \tag{2.16}$$

These are chosen such that when the system is stationary, n_j and ϕ_j obey the Josephson equation 2.11. The time dependence of the modes is captured by the scale factor $\kappa_j(t)$. We express the scaled coordinates in the $i = x, y, z$ direction as

$$\tilde{x_i}(t) = \frac{x}{b_i(t) R_i(0)}\ , \tag{2.17}$$

where $R_i(0)$ are the dimensions of the condensate as measured from the centre, and $b_i(t)$ time dependent amplitudes. From rotational symmetry we can deduce $R_x(0) = R_y(0) = R_\rho(0)$. Substitution of our anzats into equation yields

$$L_A = \pi U_0 R_\rho \sum_{ij} \Big(\frac{Q_{ij}}{2} b_x b_y b_z [\dot{\kappa_i}\dot{\kappa_j} - \Gamma_{ij}(t)\kappa_i\kappa_j] + \frac{U_0 \lambda^2}{2m R_\rho(0)^2} \frac{b_x b_y}{b_z} \sum_k M_{ijk} \dot{\kappa_i} \kappa_j \kappa_k \Big). \tag{2.18}$$

The ρ dependence has been integrated out, leaving us with the integrals

$$T_{ij} \equiv \int_{-1}^{1} \mathrm{d}\tilde{z} (1 - \tilde{z}^2) L_i^{'}(\tilde{z}) L_j^{'}(\tilde{z}), \tag{2.19}$$

$$Q_{ij} \equiv \int_{-1}^{1} \mathrm{d}\tilde{z} (1 - \tilde{z}^2) L_i(\tilde{z}) L_j(\tilde{z}), \tag{2.20}$$

$$M_{ijk} \equiv \int_{-1}^{1} \mathrm{d}\tilde{z} (1 - \tilde{z}^2) L_i(\tilde{z}) L_j^{'}(\tilde{z}) L_k^{'}(\tilde{z}). \tag{2.21}$$

And we define

$$\Gamma_{ij}(t) = \frac{\omega_z^2}{4} \frac{T_{ij}}{Q_{ij}} \frac{1}{b_x b_y b_z^3}. \tag{2.22}$$

For experimental parameters for which we have observed higher order axial modes, the magnitude of the off-diagonal elements is small compared to the diagonal. If we therefor ignore coupling between modes, we are left with

$$L_A = \pi U_0 R_\rho \sum_j \Big(\frac{Q_{jj}}{2} b_x b_y b_z [\dot{\kappa_j}^2 - \Gamma_{jj}(t)\kappa_j^2] + \frac{U_0 \lambda^2}{2mR_\rho(0)^2} \frac{b_x b_y}{b_z} M_{jjj} \kappa_j^2 \dot{\kappa}_j \Big). \tag{2.23}$$

When the rate of change of the axial oscillations is comparatively small, $\dot{b}_i/b_i/ll1$. Using the Euler-Lagrange equation and neglecting terms of $\dot{b}_i/b_i$ we find the equation of motion

$$\ddot{\kappa}_j + \Gamma_{jj}\kappa_j = 0. \tag{2.24}$$

This is a simple oscillator, in which we identify the axial mode frequency $\Omega_j = \sqrt{\Gamma_{jj}}$. This frequency is roughly half that of the drive. Our goal is to find a frame in which we can find a time independent Hamiltonian. We use the rotating wave approximation with respect to the frequency of the radial breathing mode from equation 2.7, the driving frequency ω_d.

$$\kappa = \tilde{\kappa} e^{-i\omega_d t/2} + \tilde{\kappa}^* e^{+i\omega_d t/2}. \tag{2.25}$$

When the breathing mode is weakly excited, we approximate $b_z = 1$, $b_{x,y} = 1 + A_d \cos(\omega_d t)$ and ignore second order terms or higher of A_d and $\dot{\kappa}$. This reduces the Lagrangian to

$$L_A = \pi U_0 R_\rho Q \big(\delta\omega_d \tilde{\kappa}\tilde{\kappa}^* - \frac{A_d \omega_d^2}{8}[\tilde{\kappa}\tilde{\kappa} + \tilde{\kappa}^*\tilde{\kappa}^*] - \frac{i\omega_d}{2}[\tilde{\kappa}\dot{\tilde{\kappa}}^* - \tilde{\kappa}^*\dot{\tilde{\kappa}} + A_d(\tilde{\kappa}\dot{\tilde{\kappa}} - \tilde{\kappa}^*\dot{\tilde{\kappa}}^*)] \big), \tag{2.26}$$

where we approximate the detuning with respect to the drive $\delta = \omega_d/2 - \Gamma_{jj}$, $\omega_d\delta \simeq (\omega_d/2)^2 - \Omega^2$. From here we can find the Hamiltonian via

$$H \equiv \dot{\tilde{\kappa}} \frac{\partial L}{\partial \dot{\tilde{\kappa}}} + \dot{\tilde{\kappa}}^* \frac{\partial L}{\partial \dot{\tilde{\kappa}}^*} - L. \tag{2.27}$$

In experiment only one mode is observed, so we drop the index to find for a single mode

$$H = \pi U_0 R_\rho Q \big(\delta\omega_d \tilde{\kappa}\tilde{\kappa}^* + \frac{A_d \omega_d^2}{8}[\tilde{\kappa}\tilde{\kappa} + \tilde{\kappa}^*\tilde{\kappa}^*] \big). \tag{2.28}$$

We may quantize $\tilde{\kappa} \to q\hat{a}$, $\tilde{\kappa}^* \to \hat{a}^\dagger$. Requiring $[\hat{a}, \partial L/\partial \dot{\hat{a}}] = i\hbar$, we introduce the normalization

$$q = \sqrt{\frac{\hbar}{\eta Q \omega_d}}, \tag{2.29}$$

which finally gives us

$$\hat{H} = -\hbar\delta \hat{a}^\dagger \hat{a} + \frac{\hbar\omega_d A_d}{8}(\hat{a}^\dagger \hat{a}^\dagger + \hat{a}\hat{a}). \tag{2.30}$$

This time independent Hamiltonian allows for a quantum mechanical description of the axial mode.

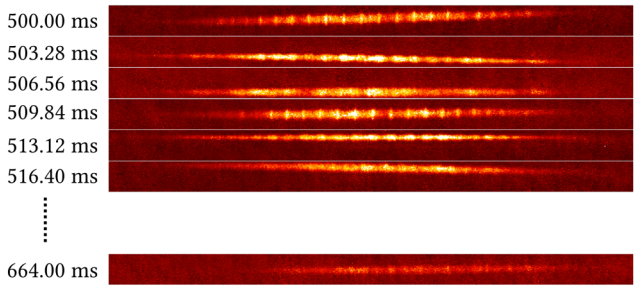

FIGURE 2.3: Image sequence of the BEC in a cigar-shaped trap after a rapid variation in the trapping potential, using off-axis holography. The oscillating width of the condensate shows the breathing mode, and a strongly excited axial mode. Image taken from ref [25].

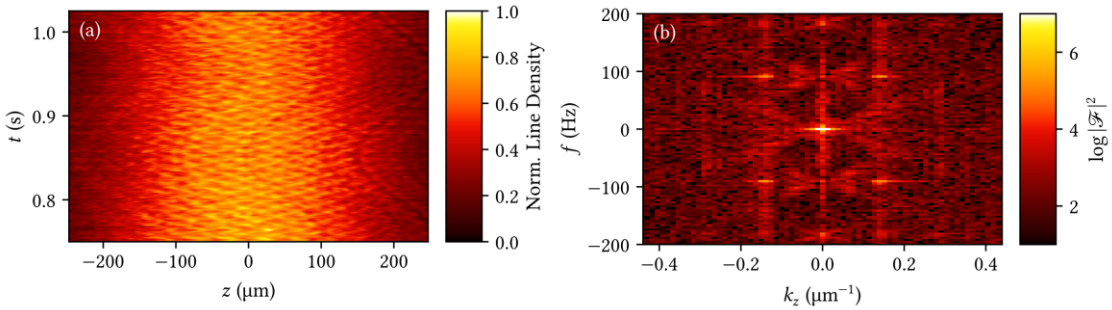

FIGURE 2.4: a) Axial density of the BEC over an extended period of time. b) The Fourier spectrum of the axial mode, the clear peaks indicating a crystalline structure. Image taken from ref [26].

2.3 Space Time Crystals

In experiments a standing wave pattern in the axial direction of the condensate was observed [8]. Later these were classified as time crystals in work by J. Smits. Figure 2.3 shows images of a high order axial mode taken at multiple times using holographic imaging techniques. To see why this can be interpreted as a crystal, we can look at how the density in axial direction evolves with time. The density profile is integrated over the radial direction and stacked over time. Figure 2.4a shows the result of this procedure, we can see a grid-like structure emerging. A Fourier analysis in figure 2.4b shows clear peaks, indicating a crystalline structure spanning the axial and the temporal dimension.

This alone does not suffice to classify the axial mode as a crystal. Crystals emerge after a phase transition, in which a symmetry of that system is broken. The Hamiltonian in equation 2.30 is invariant under $\hat{a} \to -\hat{a}$, a discrete $\mathbb{Z}_2$-symmetry. This is broken when the axial mode forms, so $\langle n \rangle \neq 0$. Upon excitation the system picks a sign, evolving with a constant phase ϕ or $\phi + \pi$ with respect to the drive. The detuning remains constant on the time scale of our experiments. To give a more intuitive picture, consider an analogy to the quantized electromagnetic field. In QED we describe the electromagnetic field as a collection of harmonic oscillators, which we excite by applying ladder operators on a ground state. Here we are describing a density oscillation on top of the Thomas-Fermi profile of the BEC as illustrated in figure 2.5. Because the temporal frequency of these density oscillations is half that of the drive, it allows for two possible modes that differ only by a phase shift π. Upon measurement, the system has to pick one of these solutions, breaking symmetry.

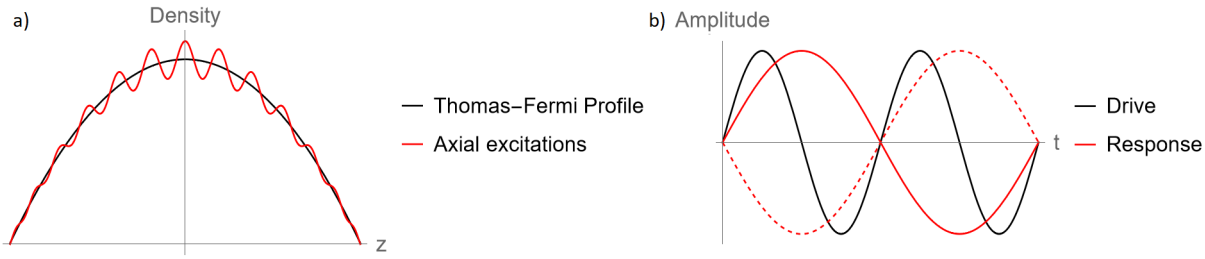

FIGURE 2.5: a) Density of the BEC in the axial direction. Black denotes the profile in stationary conditions. Oscillations with a time dependent amplitude associated with the space time crystal. b) Sketch of the response of the axial mode (red) to the driving breathing mode (black). The crystal has two solutions available, which are identical up to a phase shift.

We may expand the Hamiltonian in equation 2.30 to include a higher order term,

$$\hat{H} = -\hbar\delta\hat{a}^\dagger\hat{a}\frac{\hbar\omega_d A_d}{8}(\hat{a}^\dagger\hat{a}^\dagger + \hat{a}\hat{a}) + \frac{\hbar g}{2}\hat{a}^\dagger\hat{a}^\dagger\hat{a}\hat{a}. \tag{2.31}$$

The parameter $g = g' + ig''$ is a phenomenological parameter. The real part reflects the higher order terms we ignored in the last section. The imaginary component is required to counter exponential growth due to the presence of the drive. [26]. For time crystals with a sufficient number of quanta, $|a| \gg 1$ we can interpret a as a field. The equations of motion of a follows from the Ehrenfest theorem,

$$\frac{d\langle a\rangle}{dt} = \frac{1}{i\hbar}\langle[a, H]\rangle. \tag{2.32}$$

Applying bosonic commutation relations, we find

$$i\frac{d}{dt}a = (-\delta + g|a|^2)a + \frac{A_d\omega_d}{4}a^*, \tag{2.33}$$

$$-i\frac{d}{dt}a^* = (-\delta + g^*|a|^2)a^* + \frac{A_d\omega_d}{4}a. \tag{2.34}$$

These are the equations of motion of the field. When a random force term is added, these can be interpreted as a Langevin equation. In analogy with microscopic systems, the Langevin equations give a Newtonian description of a particle undergoing Brownian motion. The Langevin equation includes a random force term due to particle collisions, in the context of time crystals this translates as quantum fluctuations. This is missing in equation 2.34. In more recent work by Stehouwer et al. derived a field description supporting this model via a non-linear coupling with a heat bath, which is suspected to be the thermal cloud. Both a semi-classical (frequency independent) and a fully quantum mechanical (linearly dependent on frequency) approach are studied [20]. We will discuss results for the semi-classical case, corresponding with the prethermal state of the crystal. The main assumptions are as follows. In the semi-classical case, the main assumption is that the dynamics is dominated by a single frequency $\bar{\omega}$. The fluctuation-dissipation theorem is then evaluated at $2\bar{\omega}$, captured by the Keldysh function $g^K = 2ig''\frac{K_b T}{\hbar\bar{\omega}}$, at temperature T. The Fokker-Planck distribution $P[a, a^*, t]$, which describes the probability of finding the system in a state characterized by (a, a^*) is found to be

$$i\hbar\frac{\partial}{\partial t}P[a,a^*,t] = -\frac{\partial}{\partial a}\left((-\hbar\delta+\hbar g|a|^2)aP[a,a^*,t]\right) + \frac{\partial}{\partial a^*}\left((-\hbar\delta+\hbar g^*|a|^2)a^*P[a,a^*,t]\right) - \frac{\hbar g^K}{2}\frac{\partial}{\partial a^*}\left(|a|^2\frac{\partial}{\partial a}P[a,a^*,t]\right) - \frac{\hbar g^K}{2}\frac{\partial}{\partial a}\left(|a|^2\frac{\partial}{\partial a^*}P[a,a^*,t]\right). \quad (2.35)$$

In the right hand side, first order derivative terms are equivalent to the equation of motion in equation 2.34. The second order terms include quantum fluctuations into our description. We believe that these may lead to a coupling between the crystal modes, which is the focus of this thesis.

2.3.1 Phase diagram

The behaviour of the time crystal is essentially determined by three parameters, the combined drive term $A_d\omega_d$, detuning δ and the components of the noise term g. In this section we will consider the stability of the crystal with respect to these parameters. If we ignore quantum fluctuations, we can rewrite equation 2.34 as

$$\frac{d}{dt}\begin{pmatrix} a \\ a^* \end{pmatrix} = i\begin{pmatrix} -(-\delta+g|a|^2) & -\frac{A_d\omega_d}{4} \\ \frac{A_d\omega_d}{4} & (-\delta+g^*|a|^2) \end{pmatrix}\begin{pmatrix} a \\ a^* \end{pmatrix} \quad (2.36)$$

Considering equilibrium, this system of equations has non-trivial solutions only when the determinant of the matrix in the right lid is zero. This gives us

$$0 = \left(\frac{A_d\omega_d}{4}\right)^2 - \delta^2 + 2g'\delta|a|^2 - |g|^2|a|^4. \quad (2.37)$$

from which we find the equilibrium value

$$|a_{eq}|^2 = \frac{g'}{|g|^2}\delta + \frac{1}{|g|}\sqrt{\left(\frac{A_d\omega_d}{4}\right)^2 - \frac{g''^2}{|g|^2}\delta^2}. \quad (2.38)$$

We can associate equation 2.37 with an effective potential $V(|a|)$. We must have $\frac{\partial V(|a|)}{\partial|a|}\Big|_{|a|=|a_{eq}|} = 0$ at equilibrium. Since $\frac{d^2}{dt^2}|a| = -\frac{\partial}{\partial|a|}V(|a|)$, we integrate equation 2.37 to find

$$V(|a|) = -\frac{1}{2}\left[\left(\frac{A_d\omega_d}{4}\right)^2 - \delta^2\right]|a|^2 - \frac{g'\delta}{2}|a|^4 + \frac{|g|^2}{6}|a|^6. \quad (2.39)$$

The dimension of V can be converted to energy though a effective mass term $m_{eff} = 4\hbar/A_d\omega_d$, see ref [23]. This effective potential is equivalent to a Landau free energy. This describes a system with a stable and two unstable regimes, and a tricritical point at $(A_d,\delta) = (0,0)$, shown in figure 2.6. Stability can be derived by considering the extreme values of the potential. Only when there are multiple local minima and $V(|a|) > V(0)$ is the system in a stable crystalline phase. Only $g'' < 0$ will result in an equilibrium, in all other cases the crystal continues to grow exponentially. In the case where $g' = 0$, the phase boundary between the unstable and stable regime is described by the critical detuning $\delta_c = \frac{A_d\omega_d}{4}$. This is a smooth phase transition. When $g' > 0$, for $\delta < 0$ this becomes a second-order phase transition. For $\delta > 0$, the phase transition is first order and shifts to

$$\delta = \left(1 - \frac{3}{4}\frac{g'^2}{|g|^2}\right)^{-1/2}\delta_c. \tag{2.40}$$

When the system is equilibrium and if the field approximation $|a| >> 1$ holds, we can use classical statistical theory to describe the probability to occupy a state. The only degree of freedom is the number of quanta, so the probability distribution is

$$P(|a|) = \frac{\exp[-V(|a|)/2K_bT]}{Z}, \tag{2.41}$$

with $Z = \int \exp[-2V(|a|)/2K_bT]\mathrm{d}|a|$. One should note that even in an equilibrium situation, this does not capture the full probability distribution, as it only takes the number of quanta into account. Whereas previous work shows that $\arg(a)$ plays a role as well, the field of a has two degrees of freedom.

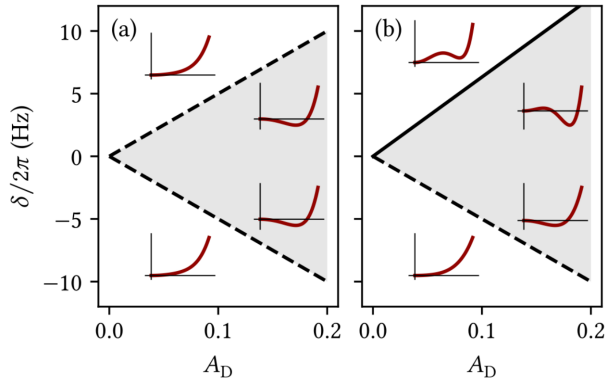

FIGURE 2.6: Phase diagram as presented by Smits [26], describing the equilibrium state of the system at $g'' = 10^{-4}\mathrm{s}^{-1}$ and $\omega_d/2\pi = 200$ Hz. Left and right show $g' = 0$ and $10^{-4}\mathrm{s}^{-1}$ respectively. Striped lines indicate smooth tricritical (left) or second-order (right) phase transitions between the stable and unstable crystal regimes. Inset are schematic representations of the effective potential, equation 2.39.

2.3.2 Line model

Calculations on the full two dimensional problem are time consuming, especially given the large parameter space. As it turns out, most of the dynamics of the probability distribution happen roughly in one direction. This was discovered in previous work by Stehouwer et al[20]. We can reduce the problem by one dimension using a toy model, simplifying the the equations while still describing the the dynamics of the overall system qualitatively. We will refer to this as the line model. We start by expressing the Fokker-Planck equation in polar coordinates $P(\rho, \phi)$, with $\alpha = \frac{\hbar\bar{\omega}}{K_bT}$,

$$\frac{\partial P}{\partial t} = -\frac{1}{\rho}\frac{\partial}{\partial \rho}(\rho A_{\rho,sc}P) - \frac{1}{\rho}\frac{\partial}{\partial \phi}(A_{\phi,sc}P), \tag{2.42}$$

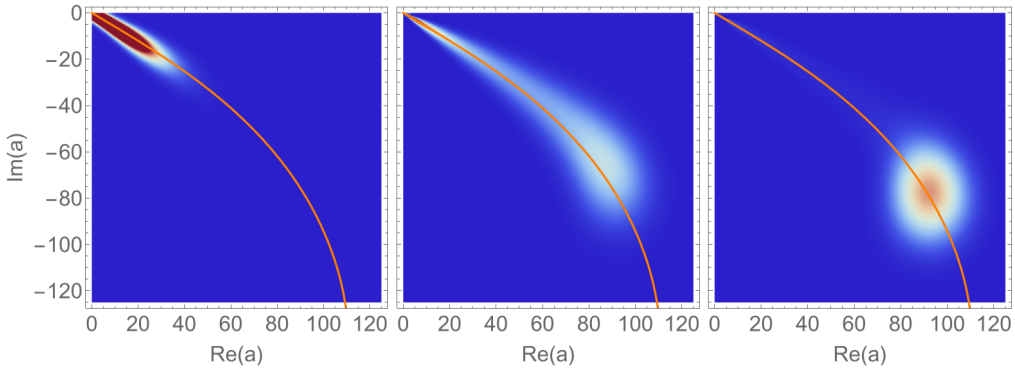

FIGURE 2.7: Simulation of $P(\rho, \phi)$ at various times using the full Fokker-Planck equation, as presented by Stehouwer et al. [20]. Imaginary axis is shared. The inset orange line is defined by zero angular flux, $A_{\phi,sc} = 0$. This line follows the general behavior of P, supporting the base assumption of the line model.

with

$$A_{\rho,sc} = g''\rho^3 - \frac{\omega_d A_d}{4}\rho \sin 2\phi + \frac{g''}{2\alpha}\rho^2 \frac{\partial}{\partial \rho}, \tag{2.43}$$

$$A_{\phi,sc} = \delta\rho - g'\rho^3 - \frac{\omega_d A_d}{4}\rho \cos 2\phi + \frac{g''}{2\alpha}\rho \frac{\partial}{\partial \rho}. \tag{2.44}$$

We can identify $A_{\rho,sc}$ as a flux current in the ρ direction, and $A_{\phi,sc}$ in the ϕ direction. In figure 2.7 we can see a 2d simulation of the Fokker-Planck distribution evolve through time. Imposed is a line at which there is no angular flux, $A_{\phi,sc} = 0$. This seems to follow the general behaviour of the probability distribution reasonably. The main idea of the line model is to restrict the Fokker-Planck equation to this line. Mathematically it follows that

$$\phi(\rho) = \pm\frac{1}{2}\arccos\left(\frac{4(\delta - g'\rho^2)}{\omega_d A_d}\right), \tag{2.45}$$

which reduces equation 2.42 to

$$\frac{\partial P}{\partial t} = -\frac{1}{\rho}\frac{\partial}{\partial \rho}(\rho A_{\rho,sc} P). \tag{2.46}$$

This equation is divergent at $\rho = 0$ due to the initial factor of $\frac{1}{\rho}$, which is problematic for numerical calculations. A more gentle form can be found by considering $P' = \rho P$. Substitution in equation 2.42 yields

$$\frac{\partial P'}{\partial t} = -\frac{\partial}{\partial \rho}(A(\rho)P'). \tag{2.47}$$

Substitution of $\phi(\rho)$ and using the identity $\sin(\arccos(x)) = \sqrt{1-x^2}$, the flux current reduces to $A(\rho) = B(\rho) + C(\rho)\frac{\partial}{\partial\rho}$ with coefficients

$$B(\rho) = g''\rho^3 - \frac{\omega_d A_d}{4}\rho\sqrt{1 - \frac{16(\delta - g'\rho^2)^2}{\omega_d^2 A_d^2}} - \frac{g''\rho}{2\alpha}, \tag{2.48}$$

$$C(\rho) = \frac{g''\rho^2}{2\alpha}. \tag{2.49}$$

Note that the last term of B is orders of magnitude smaller than the other terms, and can therefor be neglected.

2.3.3 Equilibrium

In general, when the current in equation 2.46 is zero the system is in equilibrium. Setting $\rho A_{\rho,sc} P = 0$ and solving for P gives

$$\ln P = -\Big(\int 2\alpha\rho + \alpha\frac{\omega_d A_d}{2g''}\frac{\sqrt{1 - \frac{16(\delta - g'\rho^2)^2}{\omega_d^2 A_d^2}}}{\rho}\partial\rho \Big). \tag{2.50}$$

Evaluation of this integral yields complex terms, which is problematic for a real valued probability function. As such, only when $g^{'} = 0$ can we find acceptable solutions. In specific regime the line model describes a constant angle $\phi = \frac{1}{2}\arccos(\frac{4\delta}{\omega_d A_d})$. The components of the current simplify to

$$B = g''\rho^3 + \sqrt{\delta_c^2 - \delta^2}\rho \tag{2.51}$$

$$C = \frac{g''\rho}{2\alpha} \tag{2.52}$$

We can again split this in a flux term B and diffusion term C . The equilibrium value of ρ can be found by setting $\frac{\partial}{\partial\rho}B = 0$, resulting in

$$\rho_{eq} = \frac{\sqrt{\delta_c^2 - \delta^2}}{|g''|}. \tag{2.53}$$

If we set $\rho_{eq} = 0$ then P must obey

$$-\frac{\partial}{\partial\rho}\ln P = \frac{g''\rho^3 + \sqrt{\delta_c^2 - \delta^2}\rho}{g''\rho/2\alpha}. \tag{2.54}$$

The solution, up to a normalization constant, is given by

$$P \propto \exp\Big[-2\alpha\rho_{eq}^2\big(\frac{\rho^2}{2\rho_{eq}^2} - \ln\rho\big)\Big]. \tag{2.55}$$

Chapter 3

Simulation Methods

To study the behaviour of the time-crystal, we work from both the Langevin and Fokker-Plank description as discussed in chapter 2. To this end, custom code was written in python. Two simulation methods where used, one for each model.

3.1 MacCormack Method

In order to study the behaviour of the scaled probability distribution P' according to the one dimensional Fokker-Planck equation 2.47, the MacCormack method was selected. This is an explicit finite difference method suitable for nonlinear differential equations. The MacCormack method consists of two steps, a predictor and a corrector step. The predictor step calculates an estimate using forward finite differences on equation 2.47. Given a grid spacing of Δx in the spatial and Δt in the time direction, distribution at position index n and time index τ is estimated as: $(P(\rho, t) = P(n\Delta x, \tau\Delta t)$, etc)

$$\overline{P'^{\tau+1}_n} = P'^{\tau}_n - \frac{\Delta t}{\Delta x}(B_{n+1}P^{\tau}_{n+1} - B_n P^{\tau}_n). \tag{3.1}$$

Both B_n and C_n remain constant arrays during the simulation, thus need only be calculated once. The Corrector step uses the backward finite difference of the predictor for spacial gradients and halves the time step for the time derivative,

$$P'^{\tau}_{n+1} = \frac{P'^{\tau}_n + P_{flux} + P_{diff}}{2}, \tag{3.2}$$

with

$$P_{flux} = \frac{1}{2}\Big(\overline{P'^{\tau+1}_n} - \Delta t(B_n * \overline{P'^{\tau+1}_n} - (B_n * \overline{P'^{\tau+1}_{n-1}})/\Delta x\Big), \tag{3.3}$$

$$P_{diff} = -\frac{\Delta t}{\Delta x^2}\Big(\frac{C_n + C_{n+1}}{2}(\overline{P'^{\tau+1}_{n+1}} - \overline{P'^{\tau+1}_n}) - \frac{C_n + C_{n-1}}{2}(\overline{P'^{\tau+1}_n} - \overline{P'^{\tau+1}_{n-1}})\Big). \tag{3.4}$$

In contrast to implicit methods, explicit methods are easier to implement but can become numerically unstable. This is largely dependent on the size of the discretization dx, dt. A common measure for instability is the Courant measure M_c, in this system defined as

$$M_c = \frac{B_n \Delta t}{\Delta x}. \tag{3.5}$$

In order for a simulation to be stable, we need $M_c < 1$ in the entire simulated regime. In practise we require $M_c < 0.1$. As one can see, in a parameter regime with large

flux one needs to decrease Δt and thereby lengthening the simulation time, or decrease spatial resolution by increasing Δx. This may be extended to the full two dimensional problem in equation 2.42, which was done in previous work by P. Van der Straten [20].

3.2 Runge-Kutta

The equation of motion of the field a requires a different approach. The fourth order Runge-Kutta method was selected, which is a explicit method. With an error in the order $O(dt^5)$ it is a fairly stable method. In general formulation, a function y changes according to

$$\frac{\partial y}{\partial t} = f(y,t). \tag{3.6}$$

Over a timestep $t_{n+1} = t_n + \Delta t$, the function is predicted to change according to the weighted sum of four increments,

$$y_{n+1} = y_n + \frac{h}{6}(k_1 + 2k_2 + 2k_3 + k_4), \tag{3.7}$$

with

$$\begin{aligned} k_1 &= f(t_n, y_n) \\ k_2 &= f(t_n + \Delta t/2, y_n + \Delta t k_1/2) \\ k_3 &= f(t_n + \Delta t/2, y_n + \Delta t k_2/2) \\ k_3 &= f(t_n + \Delta t, y_n + \Delta t k_3). \end{aligned}$$

The k_i terms can be interpreted as different slopes of intermediate steps, as depicted in figure 3.1. They may be derived by Taylor expanding $\frac{\partial y}{\partial t}$ and ignoring explicit time-dependence of the Jacobian in higher order substitutions. Full derivations are readily available, so we will not go into detail here [27].
Starting from a single point without quantum fluctuations, the Langevin equation 2.34 gives a single deterministic path. In order to include fluctuations, we include Stratonovich multiplicative noise [26],

$$F = \tilde{R}\sqrt{\frac{2g''(N_f + 1/2)}{\Delta t}}, \tag{3.8}$$

where $\tilde{R}$ is a random variable with Gaussian spread that is redrawn at the beginning of each timestep. We evaluate a_n with equation 3.7, using

$$f = -i(-\delta + g|a_n|^2)a_n - i\frac{A_d\omega_d}{4}a_n^* - ia_n^*F. \tag{3.9}$$

The resulting set $\{a_n\}$ we refer to as a path or quantum trajectory. To achieve reliable statistics, the typical number of paths simulated is around 10^4 to 10^5.

3.3 Data storage

Every simulation outputs a datafile (*.dat*) that contains two header with simulation parameters. Programming parameters such as simulation time and grid size are

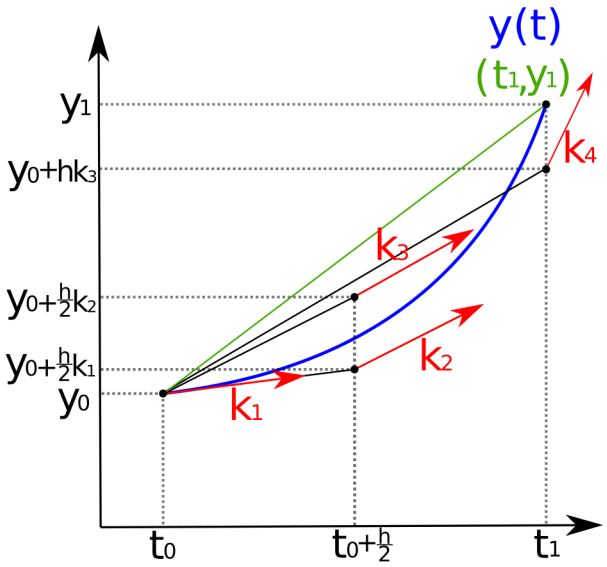

FIGURE 3.1: Geometric representation of the Runge-Kutta 4 method. A function $Y(t)$ is approximated over a timestep h with a weigted average of intermittent slopes. Image sourced from ref [28].

stored in the first. Physical parameters such as driving amplitude and detuning are stored in the second. This data is stored locally and analyzed with separate scripts. Because storage space is limited, data is stored intermittently.

Chapter 4

Simulation Results

4.1 Line Model

The first model we consider is the line model. With a typical runtime of under half an hour, it appeared the most efficient way to search though the parameter space. A large number of simulations are run, the object of investigation being long term behaviour. With a drive of $A_d\omega_d = 104\,\text{Hz}$, $g = 0.6 - 2i$ mHz and $\delta = \delta_c/2$, the simulation starts out from an initial Gaussian distribution. These are the same parameters as in the simulations reported by Stehower et al.[20]. Figure 4.1 shows the first 200 ms of a single simulation, spanning 200 s. The probability distribution P' is shown at intermittent times, labelled by colour. From the initial distribution the simulation settles into an equilibrium solution. From there on out no more dynamics occur.

At half the critical detuning fraction we are far in the stable regime. Next we consider detuning fractions close to the phase boundary, other parameters are the same as before. Shown in figure 4.2a, these yield similar results. After reaching one of the equilibrium states, no oscillation between the modes is observed. Only the equilibrium state itself is influenced, moving closer to the origin and reducing the number of quanta in the crystal, at higher detuning. Finally the noise term g is investigated, figure 4.2b shows the crystal losing quanta at higher quantum noise levels. No Rabi oscillations are observed.

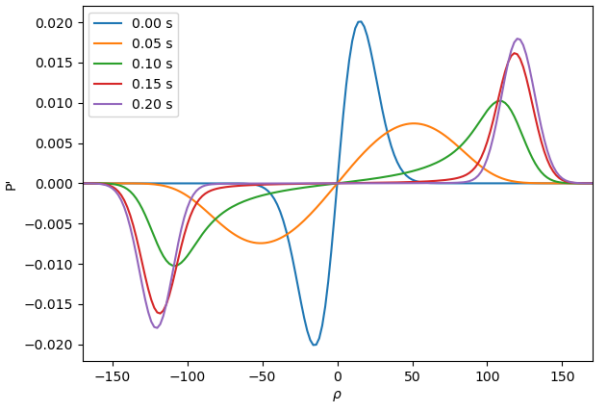

FIGURE 4.1: Time evolution of the scaled Fokker-Planck probability distribution P', from the anti-symmetric initial state at excitation until the simulation reaches an equilibrium. Colours label the evolution over time.

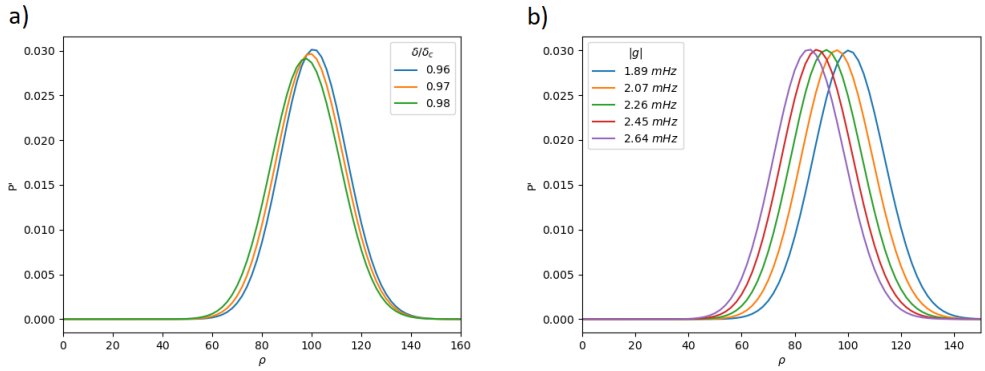

FIGURE 4.2: Final states of the scaled Fokker-Planck probability distribution P', when the simulation reaches equilibrium. We show P' at a) different detuning fractions and b) at different fluctuation strengths characterized by $|g|$. Colours label parameter values.

At higher noise levels, the simulation fails. The zero flux line that this model follows loops around back to the complex axis, setting a upper limit on the simulation boundary. The equilibrium solution violates this, as it moves beyond the upper limit for ρ. Next we set $g' = 0$, this simplification describes a constant line instead of the zero flux curve. One additional benefit is that the equilibrium can be calculated analytically in this case, as discussed in section 2.3.3. Simulations ran with an initial Gaussian distribution $P_i = \rho e^{-\alpha(\rho-\Delta\rho)^2}$. This is to insure that any probability flow though the origin is easily observable. Figure 4.3 shows three runs at different detuning fractions. A small dip at the origin is observable. In most numerical simulations, explicit methods struggle around the origin. But more suspect is the fact that the total probability, integrated over positive values of ρ does not change, i.e.

$$\frac{\partial}{\partial t}\int_0^\infty P' \, \mathrm{d}\rho = 0. \tag{4.1}$$

We therefor consider this a small numerical error. Different fluctuation strengths do not change the qualitative behaviour. Nor does lowering the driving amplitude. No probability flow though the origin is observed.

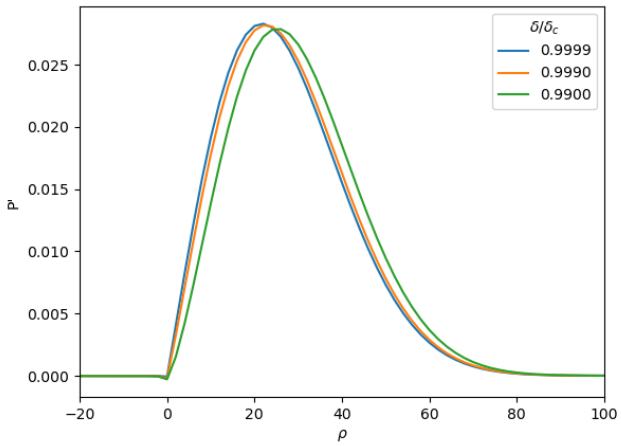

FIGURE 4.3: Final states of the normalized Fokker-Planck probability distribution P' with $g' = 0$, different detuning fractions near the phase boundary. Colours label parameter values.

4.2 Quantum Trajectories

As discussed in section 3.2, the equation of motion describing the field state of the space time crystal can be evaluated numerically. To check the validity of the code, we first make some comparisons with previous work. First we consider a simulation without fluctuations at $A_d\omega_d = 104\,\text{Hz}$, $g = 0.6 - 2i$ mHz, shown in figures 4.4a and b at 15 ms and 2 s respectively. Without quantum fluctuations all trajectories converge on two equilibrium points corresponding to the two stable crystal modes. This matches the qualitative behaviour of the quantum trajectories presented by Smits et al. [29]. When taking quantum fluctuations into account, a distribution emerges. After an initial simulated time of 200 ms in order to equilibrate, all trajectories are tallied in a histogram and presented in figure 4.5. Using data provided by Van de Straten, the Fokker-Planck probability distribution as presented in recent work by Stehouwer et al. is shown as well, allowing for direct comparison. A reasonable agreement between the models can be observed, the slight offset is attributed to the non-infinitesimal size of the histogram binning. We conclude that the code is reliable and this approximation to be suitable. Typical run-time ranges between one to several hours.

The next area of interest is close to the phase boundary. The detuning is raised to $\delta = 0.99\delta_c$, other parameters left the same. All trajectories start in a single mode, again with an equilibrium time of 200 ms. Quantum trajectories start crossing between modes, figure 4.6a shows a histogram of the trajectories spanning 1.8 s. Figure 4.6b shows a single trajectory, representative of the system. Trajectories avoid the origin and instead move around it in a counterclockwise fashion, when the detuning is chosen to be positive. Negative detuning induces clockwise motion. To investigate this further, the rate at which the trajectories cross over at a longer timescale is analysed. Assuming a constant transfer rate R, then the rate of change can be modelled as

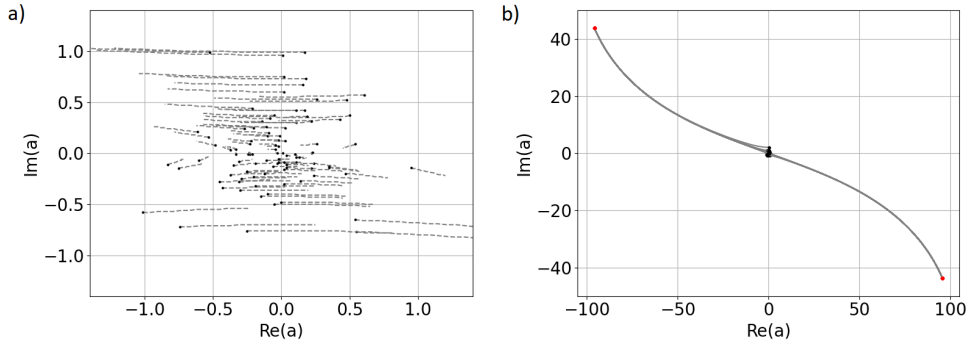

FIGURE 4.4: The evolution of several paths without quantum fluctuations, over a) 15 ms b) 2 s, from a Gaussian initial distribution. Initial and final positions are denoted with a black and red dot respectively.

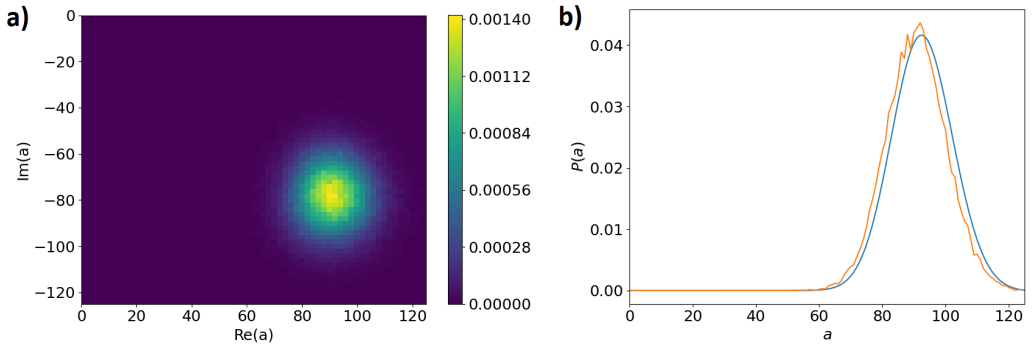

FIGURE 4.5: a) Histogram of 2000 paths, evolved over 500 ms. b) In orange, the normalized histogram at $Im(a) = -80$. In blue, the normalized simulation data as reported by Stehower et al. [20].

$$\dot{n_R} = R(n_L - n_R), \tag{4.2}$$

$$n_L(t) = \frac{1 - e^{-Rt}}{2}, \tag{4.3}$$

with $n_{L/R}$ the number of trajectories in the left and right quadrants respectively. Figure 4.7 shows this fit on a simulated runtime of 10 s. At a driving of $A_d = 0.1$, $\omega_d/2\pi = 183$Hz, $g = 0.6 - 2i$ mHz and $\delta = 0.9\delta_c$, we find excellent agreement at $R = 160.2(5)$ ms^{-1}.

Next we investigate the dependence of the transfer rate on driving parameters, the results are shown in figure 4.8. The rate decreases linearly with the driving amplitude, which correlates with the equilibrium modes being further apart in the phase space of a. As the detuning approaches the phase transition to the unstable crystal regime, the rate increases super-exponentially. This type of probability flow is reminiscent of a thermal equilibrium, rather than tunneling or a coherent oscillation. Because these might still be present but overshadowed by this thermal like interaction, we reduce the effect of noise through the g'' parameter.

At a drive of $A_d = 0.03$, $\omega_d = 2\pi \times 180$ Hz and detuning $\delta = 0.9\delta_c$, g'' is lowered to various orders of magnitude to study the effect of weak fluctuations. To get a clear picture of the behaviour in the whole phase space, trajectories are started equally

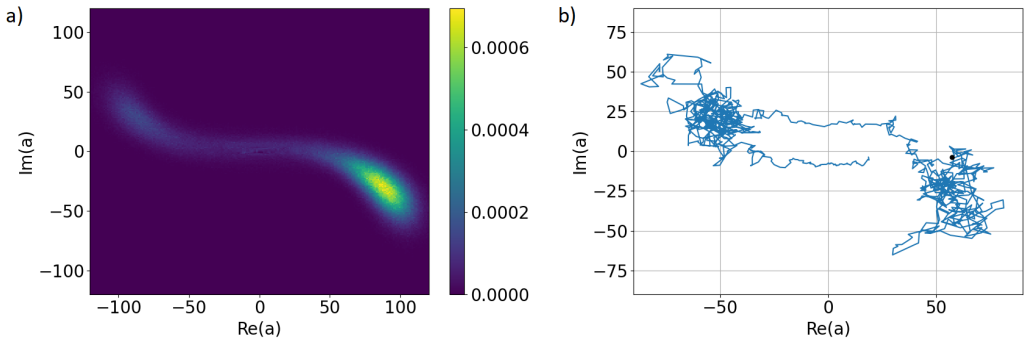

FIGURE 4.6: a) Histogram of 2000 quantum trajectories, spanning 1.8s at a critical detuning fraction of $\delta = 0.99\delta_c$. b) Typical motion of a single quantum trajectory, starting position is indicated by a dot.

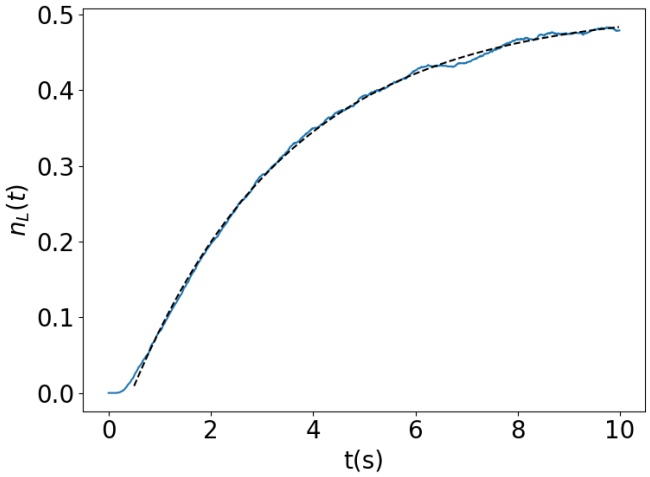

FIGURE 4.7: Fraction of trajectories n_L crossed over as a function of time, at a driving of $A_d = 0.03$, $\omega_d/2\pi = 180$Hz and $\delta = 0.9\delta_c$. Fitted with a rate of $R = 0.16\ \mathrm{s}^{-1}$.

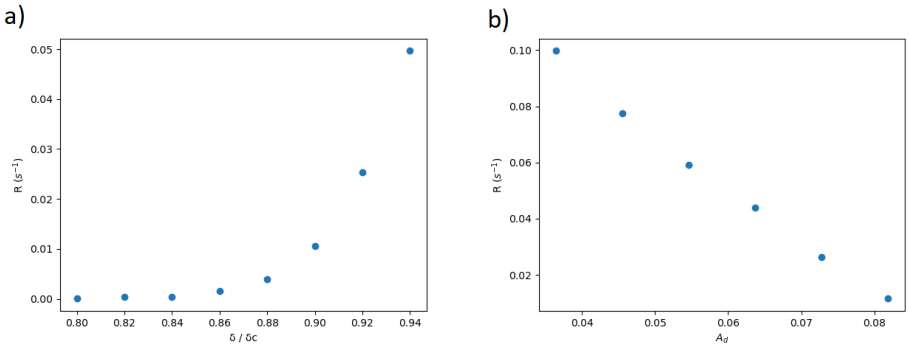

FIGURE 4.8: Transfer rate as a function of a) detuning ($A_d = 0.1$) and b) drive strength ($\delta = 0.9\delta_c$). $\omega_d/2\pi = 183$Hz. Error bars are smaller than the point size.

distributed over the imaginary axis, figure 4.9. As the fluctuation strength decreases, the system changes from being predominantly diffusive to flux current dominated. A trapping-like phenomenon starts to occur, where trajectories become confined to

orbits. In the extreme limit $g'' \to 0$, these orbits become closed and deterministic. Based on the starting point of the trajectories they are either confined to a single mode, or switch between modes in a coherent-like fashion.

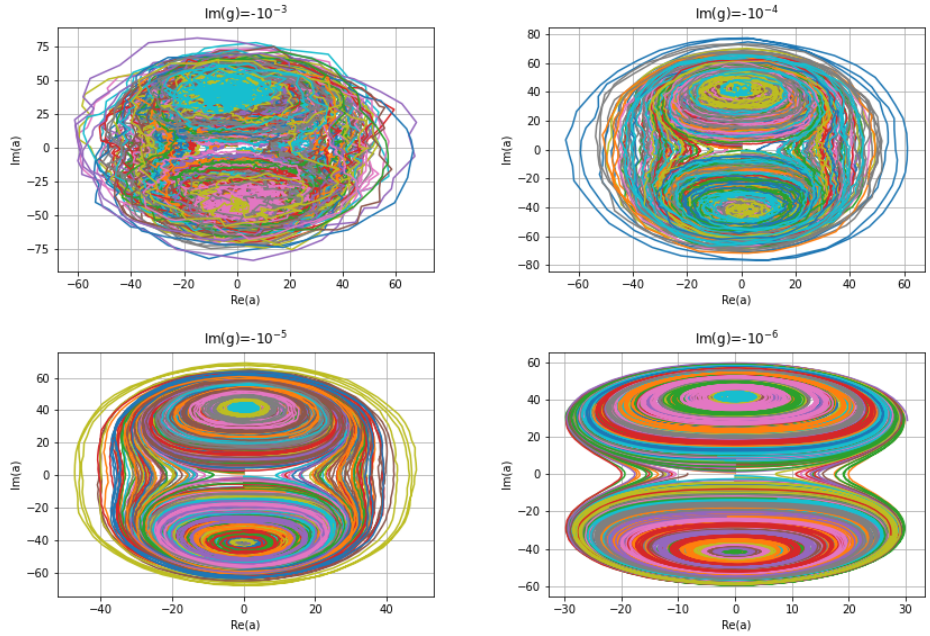

FIGURE 4.9: Trajectories starting equally distributed over the imaginary axis, at various quantum noise levels. Colours distinguish individual trajectories. System parameters are $g' = 0.01$Hz, $\delta = 0.9\delta_c$, $A_d = 0.03$, $\omega_d/2\pi = 183$ Hz.

The behaviour of these orbits is investigated further, at $g' = 0.01$Hz, $g'' = 0$. The detuning acts as an order parameter, this gives rise to a number of regimes shown in figure 4.10. For detuning corresponding to the stable regime $|\delta| < |\delta_c|$, the phase space looks the same as before. Orbits are split between three regimes, two orbiting modes and one enclosing both. When $\delta < -|\delta_c|$ there is but a single regime, wherein all orbits circle around the origin. Lastly, when $\delta > |\delta_c|$ we see four regimes. Two orbiting crystal modes, although one should keep in mind that these modes may no longer represent the time crystal modes correctly in this unstable regime. The other two regimes consist of orbits around the origin, but split apart in a regime close to the origin and one enclosing the rest.

It is important to note that $g'' \to 0$ not only kills the fluctuations, but is also changes the flux current. Figure 4.11 shows two simulations with nonzero g'' but with multiplicative noise disabled. The orbit like behaviour compared to the previous results changes significantly. Trajectories become attracted to the equilibrium points in the system. Only those starting sufficiently away from the equilibria cross over to the other mode.

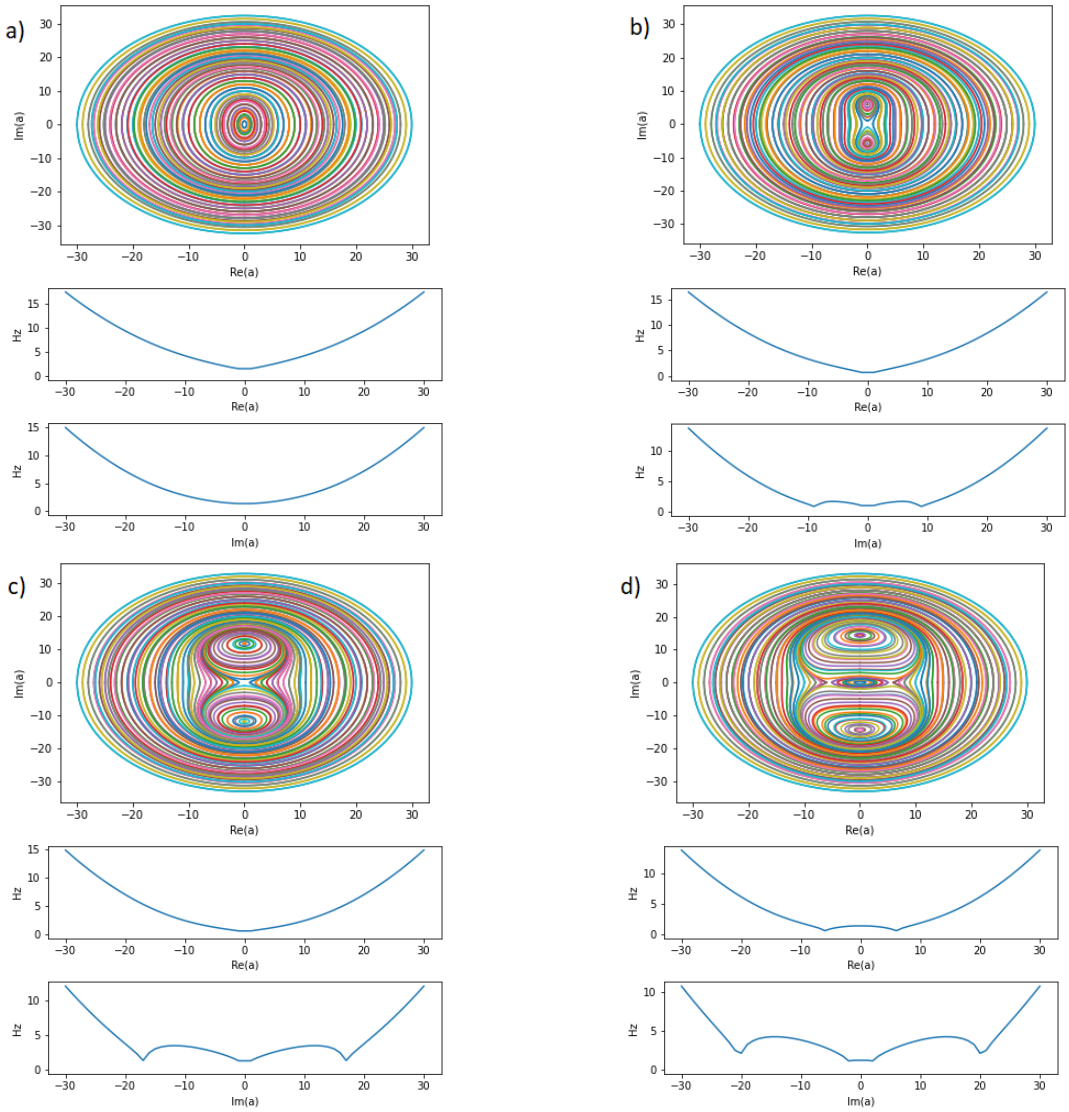

FIGURE 4.10: Orbits calculated at various critical detuning fractions at a) $-1.4\delta_c$, b) $-0.6\delta_c$, c) $0.6\delta_c$ and d) $1.4\delta_c$. Colours distinguish individual trajectories. Noise parameter is set to $g' = 0.01$Hz, $g'' = 0$. Below, orbit frequencies are plotted against initial position on the real and imaginary axis. Orbit frequency approaches zero near equilibrium points in the phase space.

4.3 Damped mode oscillations

The models presented so far are approximations of the full Fokker-Planck distribution. By extending the MacCormack method to two dimensions, we can numerically evaluate the two dimensional Fokker-Planck equation 2.35. The following section contains simulations that are written and executed by Peter van der Straten. Increasing the noise parameter g'' reveals a different picture, while g' is set to zero. Short term dynamics of the probability distribution changes significantly, compared to the previous regimes. Simulations of the 2D Fokker-Planck distribution start off in a single crystal mode. The starting distribution is approximated as Gaussian, fitted to an already equilibrated calculation. Figure 4.12 shows a non-symmetric probability flow between the modes, the total probability in the unoccupied mode exceeds

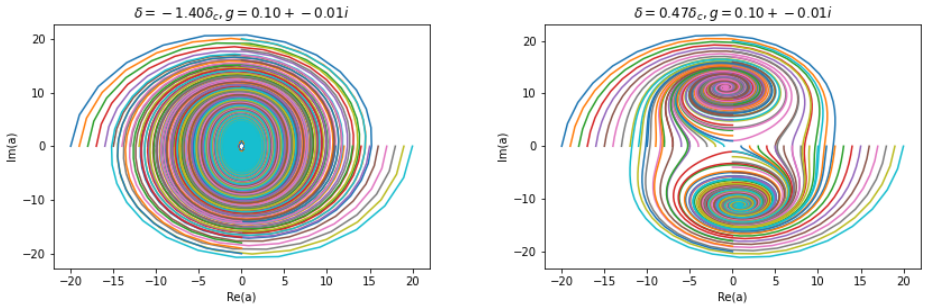

FIGURE 4.11: Trajectories without quantum fluctuations for nonzero g'', colours distinguish individual trajectories. Orbit like behaviour disappears, instead trajectories are attracted to the equilibrium points in the phase space.

that of starting mode for a limited time. At long timescale we see the two modes become symmetric again.

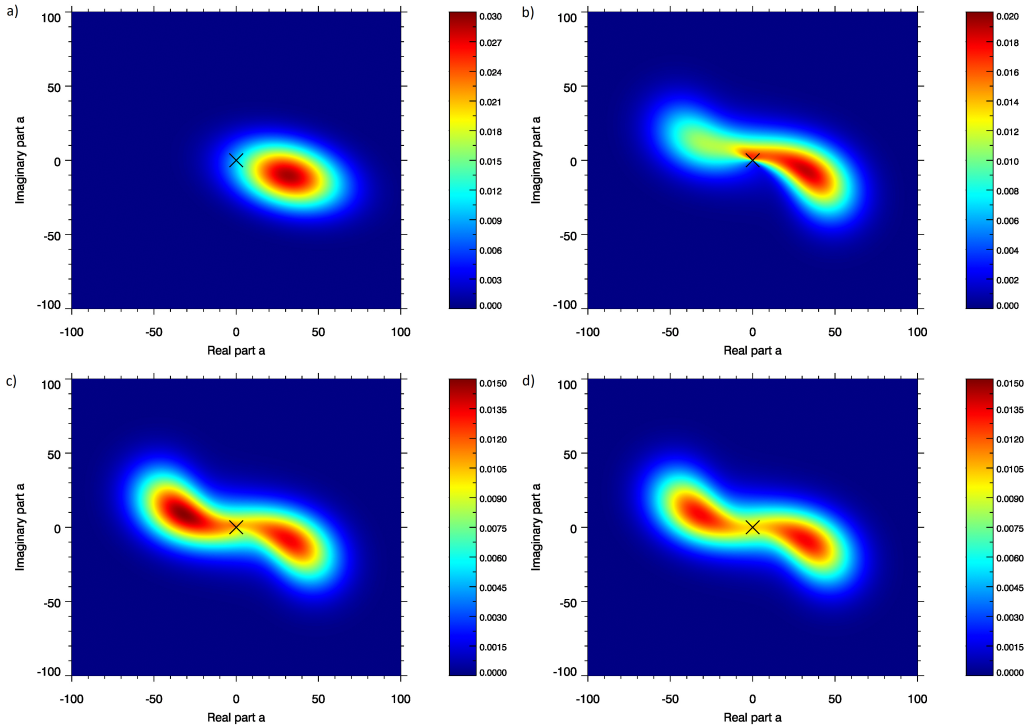

FIGURE 4.12: Fokker Planck distribution after a) 1, b) 10, c) 20 and d) 40 cycles, the time duration of one cycle is $\frac{2\pi}{\omega_d}$, approximately 5.5ms.

The probability distribution integrated over the left $Re(a) < 0$ and right $Re(a) > 0$ quadrants gives a more quantitative measure of the flow between the modes. This data is fitted a damped harmonic oscillator, characterized by a damping γ and frequency ω_0. Depending on g'' we observe two regimes, under-damped ($\omega_0 > \gamma$) and over-damped ($\gamma > \omega_0$). Figure 4.13a shows an under-damped oscillation at $g''/2\pi = -0.0025$ Hz, $A_d = 0.1$, $\omega_d = 2\pi \times 183$ Hz, $\delta/2\pi = 4.5$ Hz. We find excellent agreement at $\omega_0/2\pi = 12.48(3)$ s^{-1} and $\gamma/2\pi = 5.48(2)$ s^{-1}. We compare this with the quantum trajectory method in the same regime and find both models to converge qualitatively. After an equilibrium time of 500 ms all trajectories in the left quadrant are discarded, effectively starting the system in a single crystal

mode. The resulting observed oscillation is depicted in figure 4.14, and fitted with $\omega_0/2\pi = 17.3(2)\ \mathrm{s}^{-1}$ and $\gamma/2\pi = 9.2(1)\ \mathrm{s}^{-1}$.

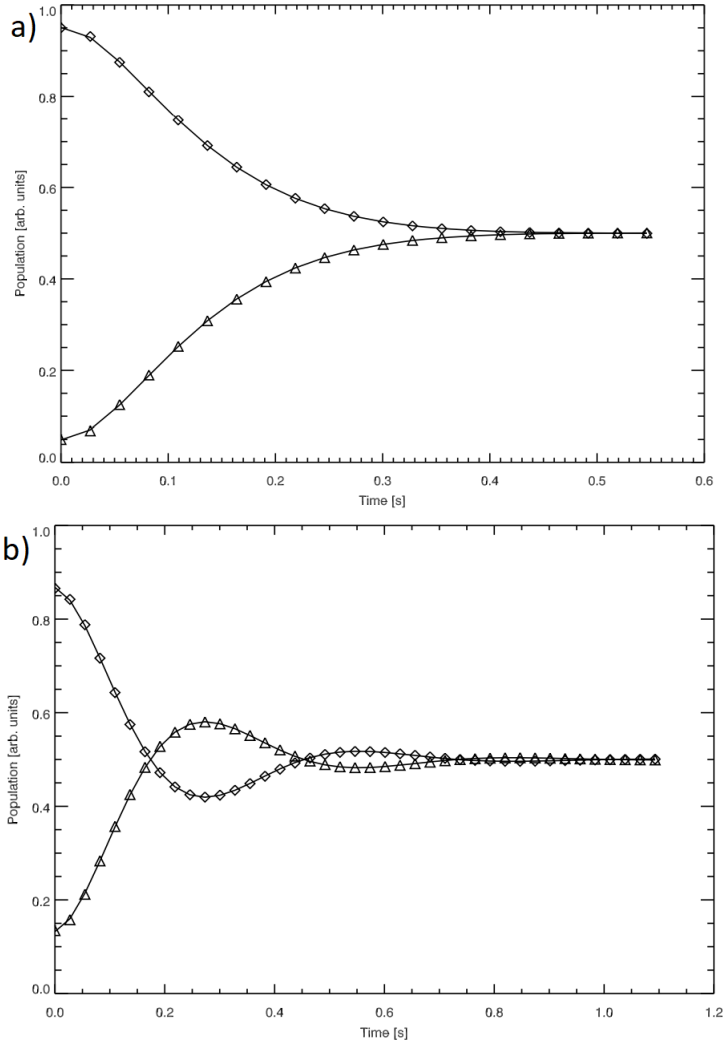

FIGURE 4.13: Integrated normalized probability distribution over the left $Re(a) < 0$ and right $Re(a) > 0$ quadrants as a function of time, denoted with a triangle and square respectively. The data is fitted to a) an over-damped harmonic oscillator at $g''/2\pi = -0.0025$ Hz and b) over-damped oscillator at $g''/2\pi = -0.01$ Hz. Driving parameters differ slightly.

In figure 4.14b we see an over-damped oscillation, at $g/2\pi'' = -0.01$ Hz and $\delta/2\pi = 3.5$ Hz. This is essentially the same behaviour we observed with the quantum trajectories in the previous section. The total probability in the unoccupied mode at the start never exceeds that of the occupied mode. We find a damping rate of $\gamma = 12.88(9)\ \mathrm{s}^{-1}$.

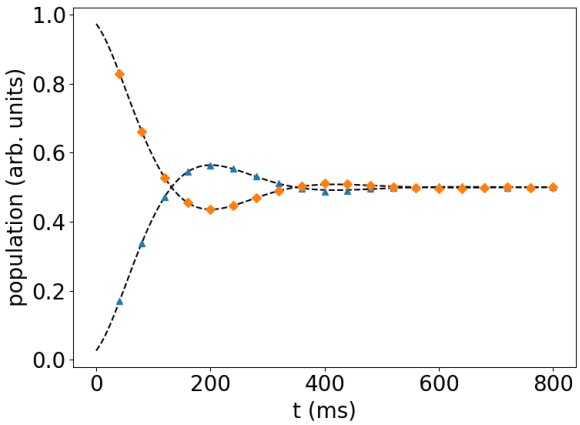

FIGURE 4.14: Normalized number of quantum trajectories in the left $Re(a) < 0$ and right $Re(a) > 0$ quadrants as a function of time, denoted with a triangle and square respectively. Calculated using identical parameters as in figure 4.13a and fitted with under-damped oscillation, indicated with a line.

Investigation of the dependence of the oscillation parameters on the driving and noise parameter yields the following results. Figure 4.15a shows a linear relation between γ and detuning δ, and a quadratic relation for ω_0, approximately. We see a crossover between over to under-damped at around $\delta = 3.4\ \mathrm{s}^{-1}$. In figure 4.15b we see a linear relation between γ and g''. Because ω_0 increases at a comparable rate, these simulations remain in the under-damped regime.

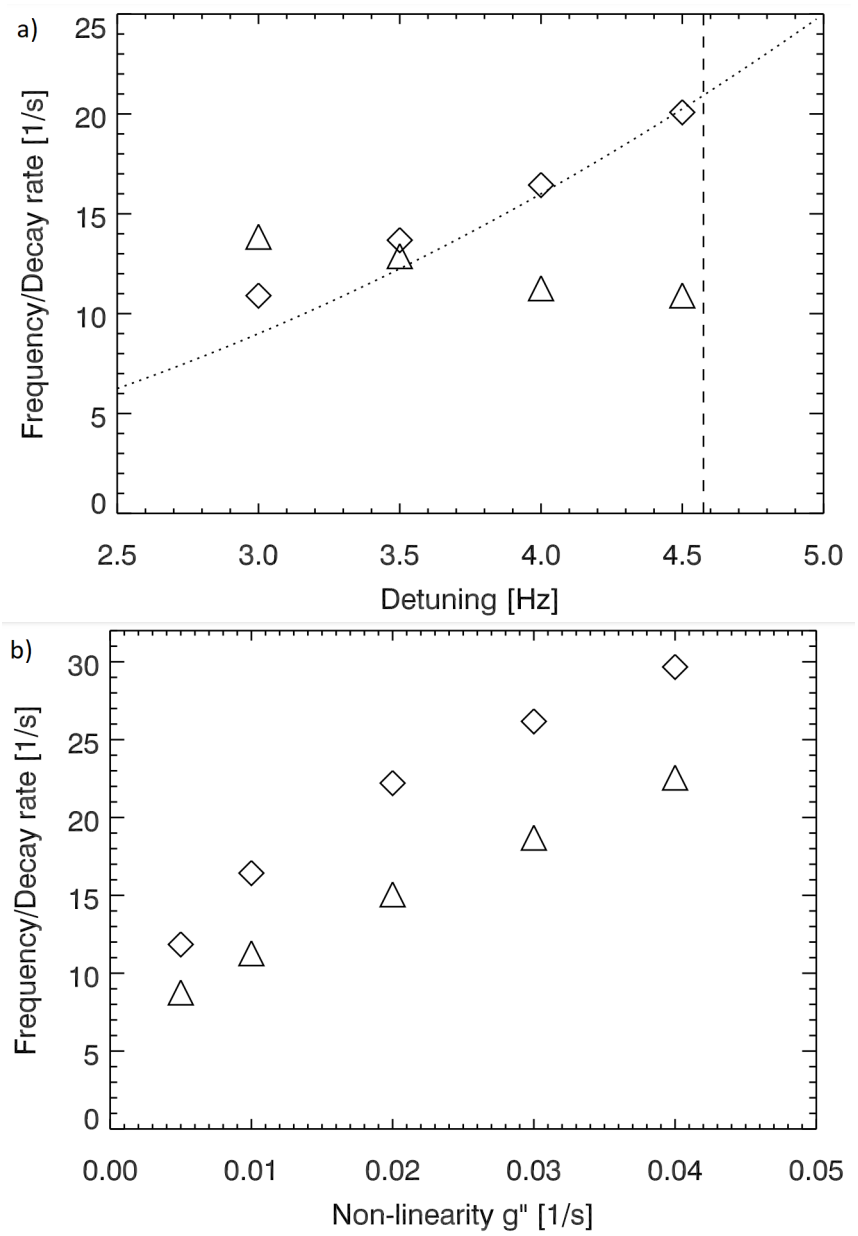

FIGURE 4.15: Oscillation parameters, as a function of a) detuning δ and b) noise parameter g''. Frequency ω_0 and damping γ are denoted with a square and triangle respectively. Striped line indicates the boundary of the stable regime, δ^2 is plotted as dotted line.

Chapter 5

Experimental Setup

5.1 Cooling

In our experimental setup we use sodium-23 atoms to create Bose-Einstein Condensates. Sodium is particularly suitable due to its D-line transitions. These fall in the visible spectrum, to which a many existing laser systems can couple. Sodium also has a good ration between two and three body collisions, which lead to more effiecient cooling. Figure 5.1 shows a schematic overview of the vacuum setup of the experiment, which consists of several stages. An oven vaporizes sodium atoms which shoot out into a Zeeman slower. After this they are collected in a magnetic-optical trap(MOT) and finally cooled in a magnetic trap (MT).

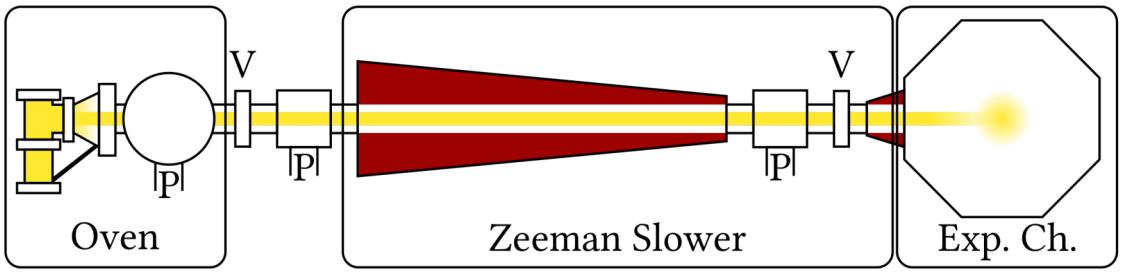

FIGURE 5.1: Schematic overview of the vacuum setup. Valves are denoted with a 'V', vacuum pumps with a 'P'. The red shaded areas indicate the coils of the Zeeman slower, width representing the density of the winding. Sourced from ref [9].

5.1.1 Source

In order to create a stream of sodium atoms, we use a recirculation oven depicted in figure 5.2. It consist of two chambers, divided by the first diaphragm. In the left chamber solid sodium is heated to 320°C under controlled pressure. Sodium vapour then exits though the diaphragm to the second chamber, then though a second diaphragm to produce a vapour beam. The second chamber serves as a cold chamber, narrowing the beam and allowing for collected sodium to be recirculated back into the primary chamber via a recirculation tube. A temperature gradient is maintained over the entire assembly to prevent accumulation of sodium in unwanted areas.

5.1.2 Slower

Atoms leaving the oven have a mean velocity around 800 m/s, which needs to be reduced to 40 m/s in order to be captured by the MOT. To this end a Zeeman slower is

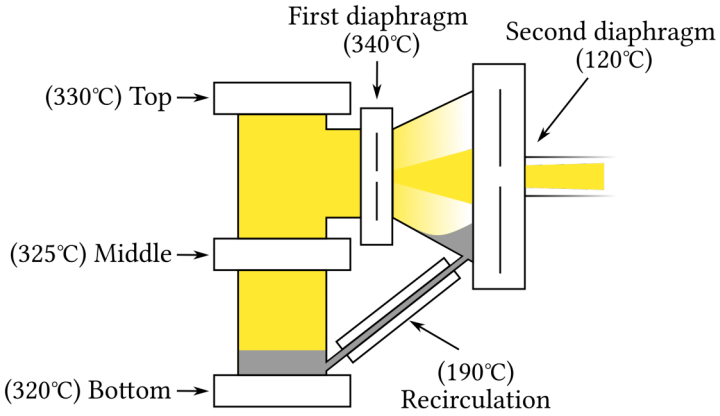

FIGURE 5.2: Schematic representation of the sodium recirculation oven. Sourced from ref [9].

used. The energy levels of sodium-23 are split up due to spin-orbit coupling, the energy levels of the hyperfine states are shown in figure 5.3. A circular polarized light beam is tuned to the transition between the $|F = 2, m_F = 2\rangle$ and $|F' = 3, m_{F'} = 3\rangle$ states. Absorption and the spontaneous remission of photons by the sodium atoms leads to a net reduction of the longitudinal velocity. The resulting change in Doppler shift is offset by a Zeeman shift induced by magnetic coils around the slower. Decay from the $F' = 3$ to the $F = 2$ state is protected due to selection rules. Due to non-linear Zeeman shifts, stray magnetic fields and imperfect polarization of the light beam, atoms can sometimes be excited to the $|F' = 2, m_{F'} = 2\rangle$ state. From here decay to the $F = 2$ state is possible, but also to the $F = 1$ ground state, dropping atoms out of the cooling cycle. To counteract this and bring the atoms back into the cooling cycle, a second beam is tuned to the transition between the ground and the $|F' = 2, m_{F'} = 2\rangle$ state.

5.1.3 Confinement

After the Zeeman slower, the particles are trapped by the MOT and form a thermal cloud. The magnetic field used to trap particles is created by two coils in anti-Helmholtz configuration. Additional rectangular coils are used to compensate the Earths magnetic field. Two retro-reflected laser beams are tuned to the $|F = 2, m_F = 2\rangle \rightarrow |F' = 3, m_{F'} = 3\rangle$ cooling cycle. One is split in the $\hat{x} + \hat{y}$ and $\hat{x} - \hat{y}$ direction, the second covers the $\hat{z}$ direction. A 1 MHz frequency difference between the beams prevents the beams from creating an optical lattice in the middle of the MOT. To prevent loss from light pressure in the centre, we use a single repump beam with a dark spot in the centre of the beam profile.

Particles in the MOT are still to energetic to form a Bose Einstein Condensate. In the last phase of cooling, atoms are confined by a magnetic field based on their dipole moment m_f. A cloverleaf arrangement of coils creates a magnetic field with a local minimum in the centre. The atoms experience an energy shift proportional to the field strength and dipole moment. The resulting trapping potential is approximately harmonic, as described by equation 2.2. Only atoms with a positive energy shift with increasing field strength can be trapped, the so-called low-field seekers $m_f = -1$. This reduces efficiency by a third, since atoms coming from the MOT are equally distributed over the $m_f = -1, 0, 1$ states. A laser pulse can be used to transfer atoms from the $m_f = 0, 1$ to the $m_f = -1$, and the MOT beams can depump

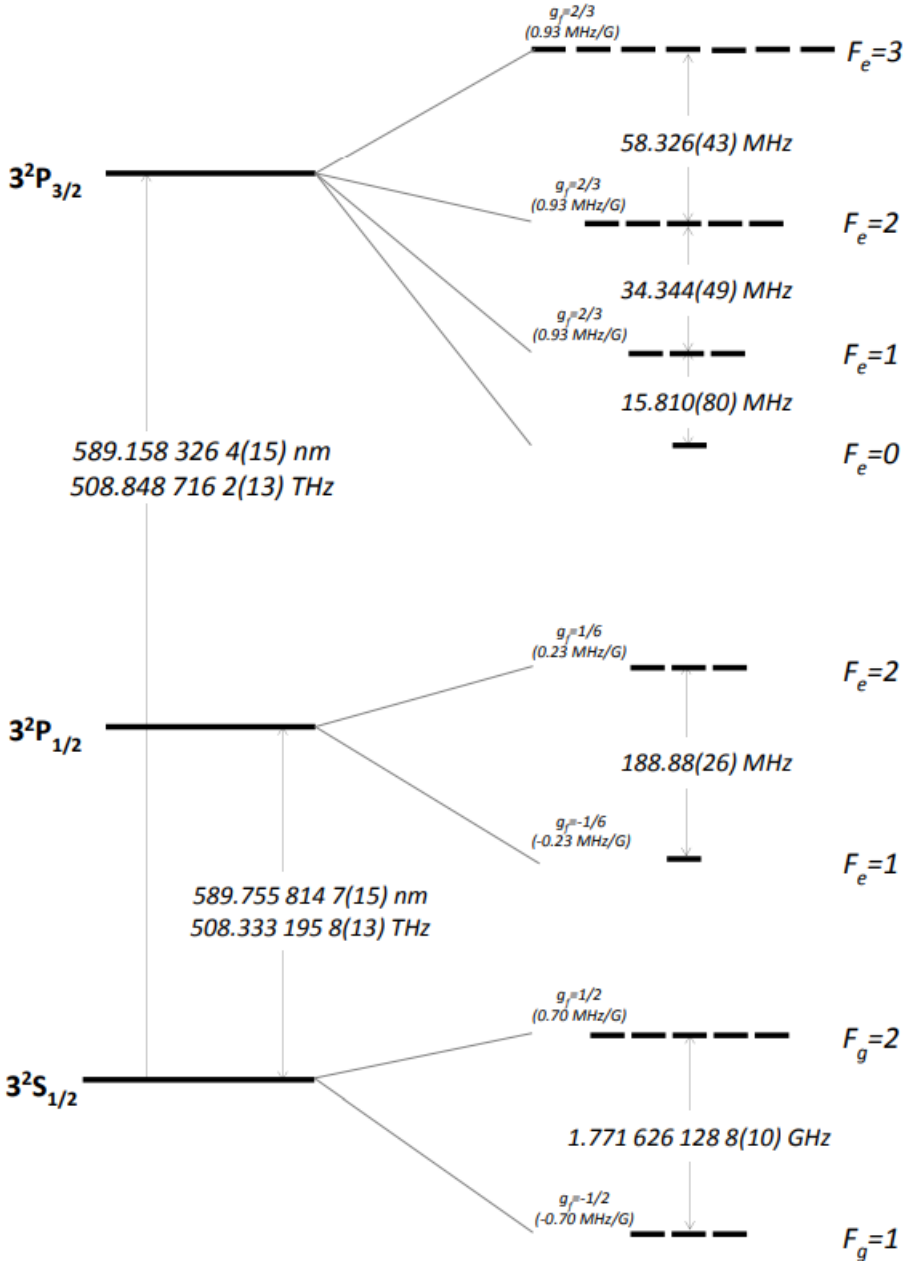

FIGURE 5.3: Hyperfine splitting of Sodium-23. Sourced from ref [8], [30]

particles in the higher $|F = 2, m_f\rangle$ states, improving the particle count to approximately two thirds. It is essential to prevent transitions from the trapped to the other states. These transitions are called Majorana flops, and occur when the magnetic field rotates faster then the precession of the magnetic moments of the trapped particles. To reach the transition temperature of the BEC, we use evaporative cooling. Using radio frequency (RF) radiation, atoms can be selectively removed by inducing a transition into a high-field seeking state (figure 5.4). The resonance frequency of the atoms is proportional to the local strength of the magnetic field and in turn to that of the potential energy of the atoms. The most energetic particles have the highest resonance frequency, to which the RF field is then tuned. The system is allowed to rethermalize after the particles have escaped. The process is repeated until the

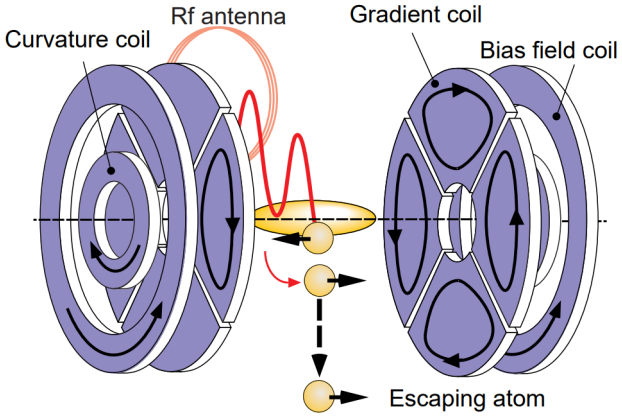

FIGURE 5.4: Schematic representation of a cloverleaf trap. Evaporation is done by selectively spin-flipping atoms into untrapped states with RF radiation. Sourced fom ref[31].

average temperature of the cloud drops below the critical temperature and the BEC forms.

5.2 Imaging

We employ two imaging techniques to get information on both the thermal cloud and the BEC. A more detailed discussion on these methods can be found in references [9], [23], [32].

5.2.1 Time-of-flight Imaging

The first method available to us is absorption imaging. The atoms are released from the trap. After a predetermined time, a laser beam tuned to the D1-Line transition illuminates the condensate and casting a shadow on a camera. The beam profile is significantly larger then the size of the cloud, such that at the position of the cloud the beam profile is approximately flat. The atom cloud absorbs and scatters light proportional to the local density. The shadow cast on the camera then allows us to calculate the density integrated over the path of the light, a column density. When the density is too low the signal-to-noise ratio becomes problematic. On the other hand, when the density is to high the cloud becomes opaque to the light beam, saturating the camera. Releasing particles from the trap allows us to control the density by varying the time of flight (TOF), such that we always image at a suitable density. Adding energy though photon absorption knocks particles out of the condensate, making this a destructive imaging technique. It gives us a measure of the particle number in both the thermal cloud and BEC, which is useful in calibration.

5.2.2 Off-axis-holography imaging

In situ observation of a time crystal requires a nondestructive method. A probing beam strongly detuned from any resonant sodium transitions can be used to image the condensate. Because the refractive index of the BEC depends on the local density, the accumulated phase of a light beam crossing though the condensate gives a quantitative measure of the column density. To prevent heating up the BEC the intensity of the probe beam must be kept low. Alone, this would give a signal too

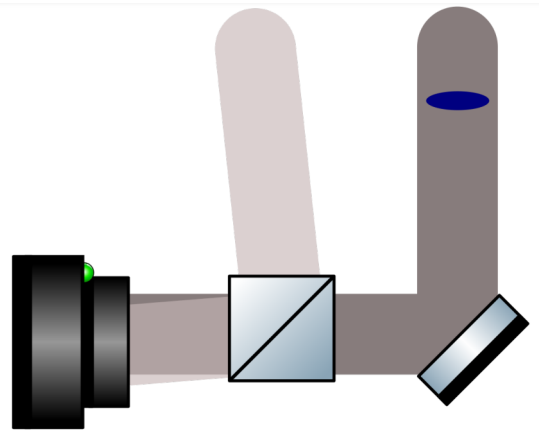

FIGURE 5.5: Schematic representation of the OAH setup. A off-resonant probe beam passed though the condensate and is collected on a camera. A mode-matched reference beam is aimed at the camera under an angle, creating an interference pattern. Image taken from ref [32].

weak to be useful. Off-axis holography allows us to increase signal strength without increasing the probe beam intensity. A second (and optionally, third) beam is mode-matched to the probe beam and projected on the camera under an angle, creating an interference pattern, schematically shown in figure 5.5
The intensity on the camera on the camera plane $\mathbf{r}$ is proportional to

$$I \propto |E_{probe} e^{i\mathbf{k}_{probe}\mathbf{r}} + E_{ref} e^{i\mathbf{k}_{ref}\mathbf{r}}|^2. \tag{5.1}$$

The cross-terms of this equation carry the information of the probe beam, with an intensity that is proportional to $|E_{ref}| = \sqrt{I_{ref}}$. By increasing the reference beam power we can improve our signal strength at no cost to the condensate. Mathematically this cross-term corresponds to a translation in Fourier space. To retrieve the phase and intensity of the probe beam, we go though the steps outlined in figure 5.6. First the stored camera image is Fourier transformed. The resulting Fourier space is then cut around $\mathbf{k} = \mathbf{k}_{probe} - \mathbf{k}_{ref}$ and translated to the origin. An inverse Fourier transformation returns the field of the probe beam, scaled by the intensity of the reference beam. Optionally we can use the Beam Propagation Method to numerically refocus the image, to correct for misalignment in the setup[33].

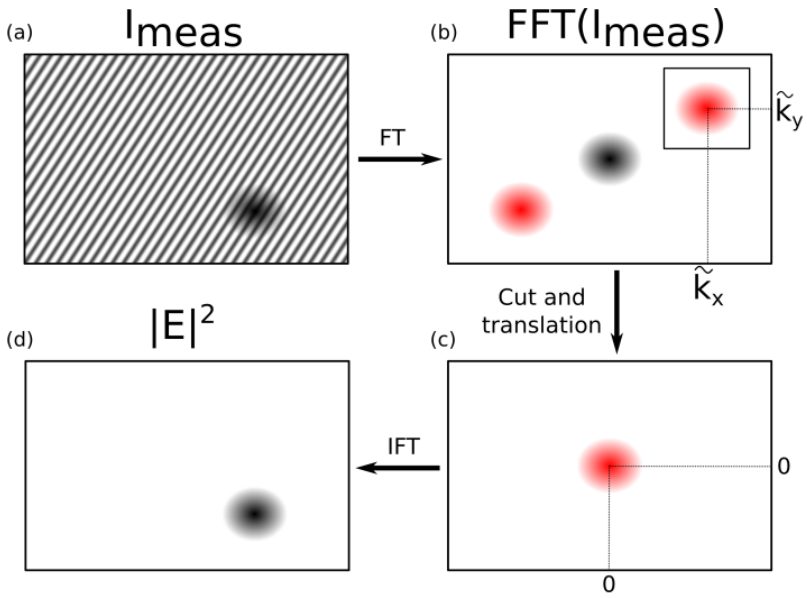

FIGURE 5.6: Schematic representation of the OAH scheme. Image taken from ref [32].

Chapter 6

Discussion

6.1 Line model

As we have seen in section 2.3.2, the one dimensional models consistently failed to produce any sort of probability flow between modes. However, the behaviour of the equilibrium distributions does match what we would expect from theory. In figure 6.1 we can see how the equilibrium distribution of the toy model for $g' = 0$ behaves, compared with our expectation based on the effective potential. The distribution moves closer to the origin when g'' becomes larger, increasing diffusion, and when $\delta \to \delta_c$. Away from equilibrium both models are in agreement, but the behaviour around the origin is different. The Fokker-Planck equation pushes P to zero near the origin, whereas the effective potential does not have the same divergence in the exponent. If we consider the flux and diffusion currents in equation 2.52, the flux current pushes P away from the origin, only diffusion can move P towards and over the origin. Except if we look at the relative strength between these two, $\frac{B}{C} \propto \frac{1}{\rho}$ near zero, which diverges. It is impossible for diffusion to overcome the flux current. This is likely where this model fails, near $a = 0$. This is also where the continuum approximation is violated. The goal of the line models is to create an efficient numerical algorithm which with to search the parameter space of our system for mode interactions. Based on the results so far, simplifying the system to one dimension seems to be an unsuitable approach if the goal is to explore dynamics between crystal modes. It does however allow for an approximate analytical solution for the equilibrium mode, which can be useful from a theoretical standpoint.

6.2 Two dimensional models

The quantum trajectories provide a number of interesting results. First, we do observe probability flow between the modes. When crossing between the modes they avoid the origin, instead moving around it in a (anti)clockwise motion. This is a further indication that the line model fails to describe the dynamics around the origin accurately. The base assumption of the line model is that the dynamics on the zero angular flux line approximately describe that of the overall system. This line passes through the origin. The fact that all quantum trajectories do not pass through the origin show that this assumption is incorrect. The (counter)clockwise motion when crossing can be understood by considering the Langevin equation (2.34). If we consider terms linear in a, then the equation reduces to $\dot{a} = -i\delta a$ for small a, a simple rotation in the complex plane depending on the sign of δ.

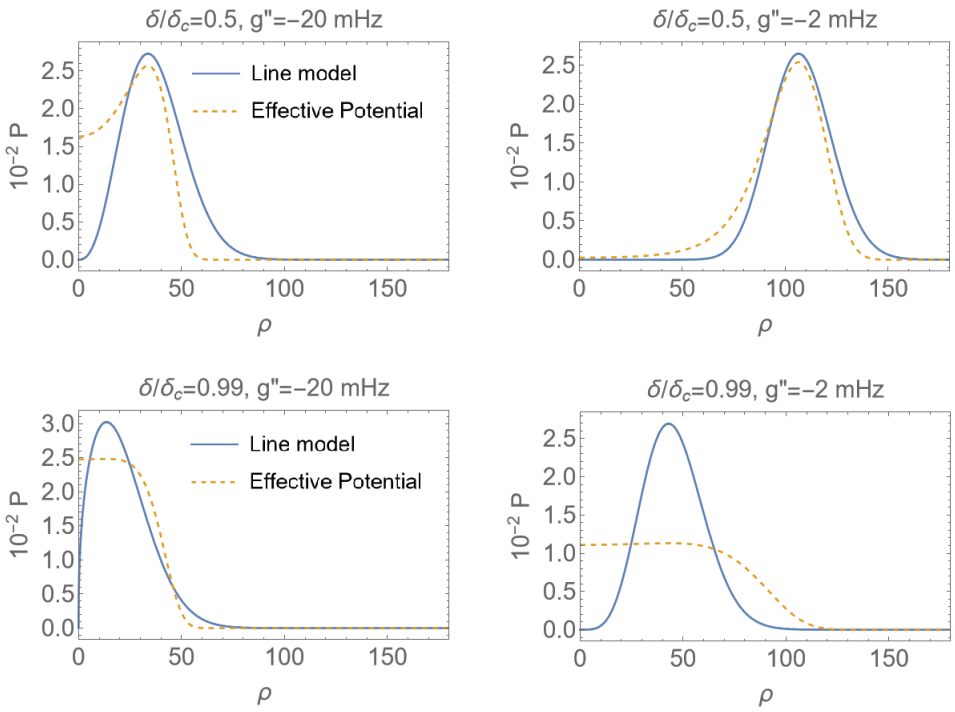

FIGURE 6.1: Equilibrium distribution in various parameters. In blue, as predicted by the Fokker-Planck line model. In orange, the effective potential as described by equation 2.41. Detuning fraction and noise parameter values are shown in graph.

6.2.1 Closed orbits

In the limit $g'' = 0$ we see closed orbits emerging, which are confined to different regimes in the phase space of a, depending on the driving parameters. For some initial values of a we observe orbits that rotate around equilibrium points of the time crystal, such that the time average $\langle |a| \rangle \neq 0$. This is reminiscent of self trapping. The question is, can we categorise it as such? In recent work by the Oberthaler group, a BEC of Rubidium atoms is confined in a double-well potential [34]–[36]. The population of the two wells displays oscillations that fall in two regimes, Rabi oscillations and self trapping, shown in figure 6.2a and figure 6.2b respectively. The interaction strength between the wells determines in what regime the system exists. The relative population difference z between the two wells is key. In the Rabi regime, the time average $\langle z \rangle = 0$. This changes in the self-trapping regime. The Bloch sphere in figure 6.2 shows oscillations with $\langle z \rangle \neq 0$ are possible, depending on the initial population imbalance. On the surface, this seems similar to the regimes we observe in figure 4.10. The detuning determines the regime, i.e. whether there are self-trapped orbits and for what range of initial values, and the initial value of a the orbit itself.

There are a number of issues with this interpretation. The crystal modes we describe are not occupied by different populations at the same time, doing so violates the symmetry breaking criterion of the time crystal. This makes the analogy between a and z problematic. The theoretical description is also considerably different. The population of the BEC in the two wells is described by a two dimensional Fock space. On the other hand, our description assumes only one dominant crystal mode

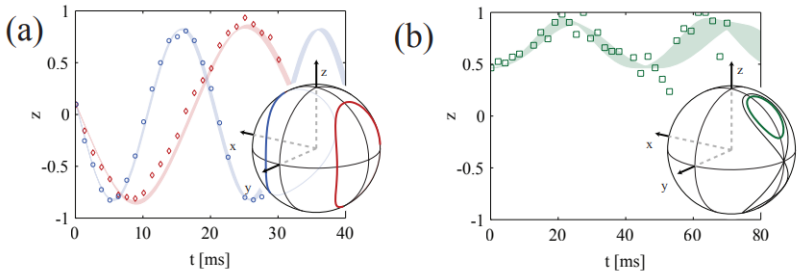

FIGURE 6.2: Bloch sphere representation of population difference z between two wells, showing in a) Rabi oscillation with $\langle z \rangle = 0$ and b) self-trapping with $\langle z \rangle \neq 0$. Image adapted from Zibold et al.[34].

frequency, resulting in effectively a one dimensional Fock space. These major differences mean that we can not regard these orbits as self trapping. From a physical standpoint, the limit $g'' = 0$ is problematic as well. As we discussed in Chapter 2, $g'' \geq 0$ leads to unlimited growth in the number of quanta of the crystal. Second, the concept of an equilibrium distribution breaks down. The collective behaviour of the quantum trajectories no longer matches the Fokker-Planck description. And third, every experimental realization will have quantum fluctuations present to some degree, which destroys this orbit like behaviour as we can see in figure 4.11. We consider this regime therefor ill suited for experimental predictions.

6.2.2 Damped oscillations

From our simulation data we can verify the suitability of the quantum trajectory approach as an approximation of the Fokker-Planck equation. When the equilibrium modes are sufficiently far apart to prevent mode interactions, the 2d Fokker-Planck and the quantum trajectory approach reproduce the same equilibrium distributions. In light of the observed damped oscillations using both the 2d Fokker-Planck and the quantum trajectory approach, the observed probability flow at nonzero g'' in section 4.2 should be reinterpreted as an over-damped oscillation. At higher quantum fluctuations both models predict an under-damped oscillation between the crystal modes. The fitted oscillation parameters lie within a factor of two, so the models agree only quantitatively. What we do not know, is if the quantum trajectory method gets the scaling of the fitted oscillation parameters with the system parameters correctly. We should note that in the under-damped regime studied using the 2d Fokker Planck method, the decay rate and oscillation frequency do not diverge near the phase transition boundary. No calculations using the quantum trajectory method have been done in this regime. And the other way around, we do observe divergence in the over-damped regime using the trajectory method, which needs to be verified with the 2d Fokker-Planck method. Even so, the results we have discussed so far support the quantum trajectory approach as a viable tool to study the parameter space of our system, even if only quantitatively.

We do not yet have a theoretical model with which to compare the oscillation parameters. Both the damping γ and oscillation frequency ω_0 above $g'' = 0.01$ s^{-1} have seemingly have a linear dependence on g''. Determining the scaling for smaller values of g'' will require more simulations. Clearly, quantum fluctuations play a major role in mode switching. Only when $\omega_0 \geq \gamma$ will we observe under damped oscillations. Given that ω_0 scales approximately with δ^2 whereas γ remains fairly constant, the detuning determines the type of oscillation between the crystal

modes. One promising lead is a Bogoliobov expansion on the Langevin equation of motion, discussed in appedix B. It gives a dispersion relation for the oscillation frequency at the correct order of magnitude, as well as the correct scaling with driving parameters. At the moment of writing, this is still work in progress.

A possible interpretation of the observed damped mode oscillation is a damped Rabi oscillation. These are not new in physics. For example, a two level system coupled to a single-mode electromagnetic cavity will undergo vacuum Rabi oscillations that display a similar damping due to relaxation; spontaneous emission and non-radiative decay [37]. In the context of time crystals, little is yet known. Theoretical work on Floquet time crystals predict Rabi oscillations in the absence of driving[38] or at differently evolving phases [39]. Neither apply to our system, or have been observed experimentally. In our system γ mostly determined by g'', suggesting that the thermal cloud is responsible for damping on our system. The origin of the coupling between the crystal modes is unclear. To the authors knowledge, this might be the first indication of a damped Rabi oscillation in a driven time crystal in a non-dissipative system. Before we can make this claim, we need a theoretical model that fits the oscillation parameters, and sheds light on the coupling between the crystal modes.

6.2.3 Experimental realization

The physical implication of mode switching is as follows. If after creating and imaging the crystal to determine the phase the system is allowed to go unobserved for some time, when we measure again there will be a nonzero change of finding a phase shift π with respect to the initial measurement. Any interaction that carries the phase information will project the crystal to one of its modes. If this happens frequently enough, mode switching will be suppressed. This is the well-known quantum Zeno effect. Experimental observation of both the over and under-damped oscillation may be possible, provided we insure adequate protection from unwanted interaction between the crystal and its surroundings. This would mean optically isolating the vacuum chamber to prevent stray photons from interacting with the condensate. The challenge here is to still ensure optical access for the probe and cooling beams. Secondly, stray particles in the vacuum setup will have a similar effect. Interactions with the BEC can be minimized by optimizing the vacuum.

Experimental realizations of the time crystals so far have driving parameters in the range of $A_d = 0.04$ to 0.1 and $\omega_d/2\pi \simeq 180$ Hz, similar to the values used in our calculations. They key difference are the detuning and noise parameter, δ and g''. The detuning is observed in a wide range between 0 and $0.5\delta_c$, and the g-factor typically lies in the order of $|g| = 10^{-4}$ Hz. Observation of mode switching requires an increase of about two orders of magnitude in the noise parameter. In order to observe the under-damped oscillation we require a higher detuning fraction, preferably higher then $0.8\delta_c$. We have not yet achieved experimental control over both these parameters.

6.3 Conclusions

Throughout this research, we have attempted to find a suitable approach to study switching between time crystal modes. Our goal is to determine the parameter space in which dynamics between crystal modes arise, characterise this behaviour, and provide a basis for experimental work. Numerical evaluation of the Fokker-Planck equation requires a long evaluation time. Combined with the large parameter space of our system, faster running approximations are desirable. We focus on two models. The first method is the line model, an one-dimensional approximation to the Fokker-Planck equation. The second is a quantum trajectory method, based on the Langevin equations of motion. We compare these to the (two dimensional) Fokker-Planck equation, evaluated using the MacCormack method.

The line model reproduces the correct equilibrium distribution at high number of quanta in the crystal, but fails close to the origin in the phase space of the crystal. We observe that flux current terms in the Fokker-Planck equation become dominant in this region, preventing probability flow between modes. This is further verified by the dynamics observed using the other methods, the origin is always avoided. We conclude this model to be unsuitable.

The quantum trajectory method becomes nonphysical in the limit of no damping, otherwise it reproduces the same qualitative behaviour as the 2d Fokker-Planck method. At higher noise levels we find both over and under-damped oscillations between crystal modes. Based on the 2d Fokker-Planck method, the type of oscillation depends largely on the detuning of the crystal with respect to the breathing mode. Both the frequency and damping parameters of the oscillations scale with the noise parameter. Additional simulations are required to verify if the quantum trajectory method produces the same scaling of the oscillation parameters. Even if this is not the case, the quantum trajectory method does provide a useful way to rapidly search the parameter space.

Experimental observation of a mode switch constitutes a π shift in the phase of the time crystal, after the system is allowed to go unmeasured for some time. Apart from sufficient isolation, observation of mode switching requires control to some extend over the detuning and noise term. The first could be realized by changing the breathing mode frequency temporarily. The noise term needs to be two orders of magnitude stronger than experimental realisations so far. To this end, the influence of the thermal cloud on the noise term needs to be investigated. The parameter space of the driving parameters in which mode switching occurs, match that of current experimental realisations.

6.4 Outlook

The field of time crystals is both new and rapidly developing. In regard to our realization of time crystals, there are plenty advancements to be made. First, work on the quantum trajectory method can be expanded in two ways. The Runge-Kutta method can be expanded to include variable step-size techniques, reducing calculation time. Secondly, simulations in the under-damped oscillation regime can be done to investigate scaling of the oscillation parameters. On the theoretical side, our next goal should be to find a mathematical description that allows us to understand and describe mode oscillations. A promising candidate is a Bogoliobov expansion on the Langevin equations of motion.

On the experimental side, the question of isolating the time crystal appears most pressing. We need to investigate if we have a sufficient vacuum and can prevent enough stray photons from interacting to allow the system to go unobserved at the timescale of the damped mode oscillation. Alterations to the experimental setup may prove necessary. Gaining experimental control over detuning and the noise factor are essential. The first step to this end is to measure the frequency of the breathing mode when changing the trap frequency, after the breathing mode is induced. Once we can control the driving frequency, a number of interesting experiments open up. Temporarily changing the driving frequency results in a change in the detuning of the time crystal. Varying the driving frequency can be done in multiple ways, continuously or step-wise for example. We should study the effect of these on the shift in the detuning, to establish the best method of control. Even when the noise factor is to low to induce mode switching, with control over the detuning we can induce forced transitions. Another important step will be to study the effect of the thermal cloud on the noise parameter, which is suspected to be its origin. This can be measured by creating time crystals with different thermal cloud fractions. This can be done by terminating the cooling process before total condensation occurs. Assuming that we can raise the noise factor through the thermal cloud population, in addition to sufficient isolation, we should be able to observe mode switching. A best case scenario would even allow us to measure the quantum Zeno effect, by repeatedly measuring the crystal in a parameter regime where a second experiment without intermittent observation show mode oscillations. These last two experiments would provide strong evidence as to the quantum nature of the time crystal.

Appendix A

Line model equilibrium

The goal of this section is to study the equilibrium distribution of the toy model discussed in section 2.3.2, for general $g = g' + ig''$. Setting the flux current to zero we have

$$(B(\rho) + C(\rho)\frac{\partial}{\partial\rho})P = 0. \tag{A.1}$$

with

$$B(\rho) = g''\rho^3 + \frac{\omega_d A_d}{4}\rho\sqrt{1 - \frac{16(\delta - g'\rho^2)^2}{\omega_d^2 A_d^2}}, \tag{A.2}$$

$$C(\rho) = \frac{g''}{2\alpha}\rho^2. \tag{A.3}$$

We can isolate P by using the derivative of the log function,

$$\frac{\partial}{\partial\rho}\log(P(\rho)) = -\frac{B(\rho)}{C(\rho)}. \tag{A.4}$$

The solution to P is then given by the anti-derivative of the right lid,

$$P = A\exp\Big[-\Big(\int 2\alpha\rho + \alpha\frac{\omega_d A_d}{2g''}\frac{\sqrt{1 - \frac{16(\delta - g'\rho^2)^2}{\omega_d^2 A_d^2}}}{\rho}\partial\rho\Big)\Big], \tag{A.5}$$

with normalization constant A. The second part of the integral in this expression can be cast in the form

$$I(x) = \int \frac{1}{x}\sqrt{1 - (a - x^2)^2}dx, \tag{A.6}$$

with $x = \sqrt{\frac{4g'}{\omega_d A_d}}\rho$,$a = \frac{4\delta}{\omega_d A_d}$. Which has the analytical solution

$$I(x) = \frac{1}{2}\Big(\sqrt{1 - a^2 + 2a - x^4} - \arcsin(a - x^2) - \sqrt{1 - a^2}\,\mathrm{arctanh}(T(x))\Big), \tag{A.7}$$

$$T(x) = \frac{1 - a^2 + ax^2}{\sqrt{1 - a^2}\sqrt{1 - a^2 + 2a - x^4}}. \tag{A.8}$$

Note that $a^2 \leq 1$ in the stable crystal regime. Because the argument of the arctangent for all values of ρ obeys $T(\rho) \geq 1$, I and in turn P become complex valued. One workaround is absorbing the complex component into the normalization factor.

Appendix B

Bogoliobov Expansion

Starting from the Langevin equations,

$$\frac{\partial}{\partial t}\begin{pmatrix} a \\ a^* \end{pmatrix} = i\begin{pmatrix} \delta - g|a|^2 & -\frac{A_d\omega_d}{4} \\ \frac{A_d\omega_d}{4} & -\delta + g^*|a|^2 \end{pmatrix}\begin{pmatrix} a \\ a^* \end{pmatrix}. \tag{B.1}$$

We expand around an arbitrary point a_0 by considering a small deviation Δa,

$$a = a_0 + \Delta a, \tag{B.2}$$
$$a^* = a_0^* + \Delta a^*. \tag{B.3}$$

We assume g to be purely imaginary, substitution into the Langevin equations and only keeping linear terms yields

$$\frac{\partial}{\partial t}\begin{pmatrix} \Delta a \\ \Delta a^* \end{pmatrix} = \begin{pmatrix} i\delta - 2g''|a_0|^2 & g''a_0^2 - i\frac{A_d\omega_d}{4} \\ g''a_0^{*2} + i\frac{A_d\omega_d}{4} & -i\delta - 2g''|a_0|^2 \end{pmatrix}\begin{pmatrix} \Delta a \\ \Delta a^* \end{pmatrix}, \tag{B.4}$$

The eigenvalues of this matrix equation we shall refer to as the Bogoliobov frequencies, these are given by

$$\Omega = 2g''|a_0|^2 \pm \sqrt{-\delta^2 + (\frac{A_d\omega_d}{4})^2 + ig''\frac{A_d\omega_d}{4}(a^2 - a^{*2}) + g^2|a_0|^4}. \tag{B.5}$$

We have absorbed a constant factor i in the matrix in equation B.4. Not doing so switches the real and imaginary parts of ω. Solutions to the under-damped harmonic oscillator with a frequency ω_0 and damping constant γ are linear combinations of

$$\begin{pmatrix} \nu \\ \nu^* \end{pmatrix} = \begin{pmatrix} e^{(\gamma + i\sqrt{\omega_0^2 - \gamma^2})t} \\ e^{(\gamma - i\sqrt{\omega_0^2 - \gamma^2})t} \end{pmatrix}. \tag{B.6}$$

We can compare $Re(\Omega)$ to γ and $Im(\Omega)$ to $\sqrt{\omega_0^2 - \gamma^2}$. An open question is where to expand around, i.e. what is a_0? We can plot Ω as a function of a_0, shown in figure B.1. We see a finite oscillation frequency at a phase of $-\pi/4$, and decay to zero everywhere else. We should note that for the system parameters used here, the average of the equilibrium distribution lies close to $-\pi/12$, at $a = 23.5 - 5.8i$, based on the quantum trajectory calculation as presented in figure 4.14. Damping is present everywhere in the phase space, and weaker near the origin.
The correct value of a_0 will depend on the system parameters. As a rough approximation, we take it to be constant at $a = 25e^{i\pi/4}$ and plot this against the oscillation parameters as presented in figure 4.15. Figure B.2 shows promising results, we can

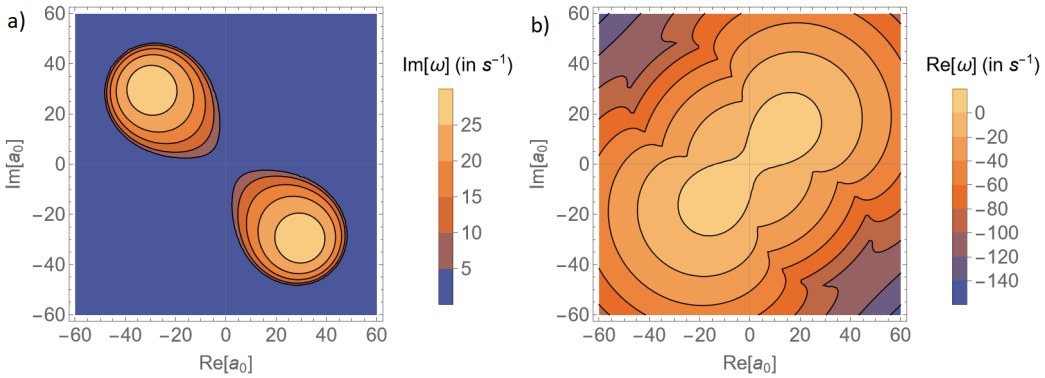

FIGURE B.1: The a) imaginary and b) real components of the Bogoliobov frequency, as a function of a_0

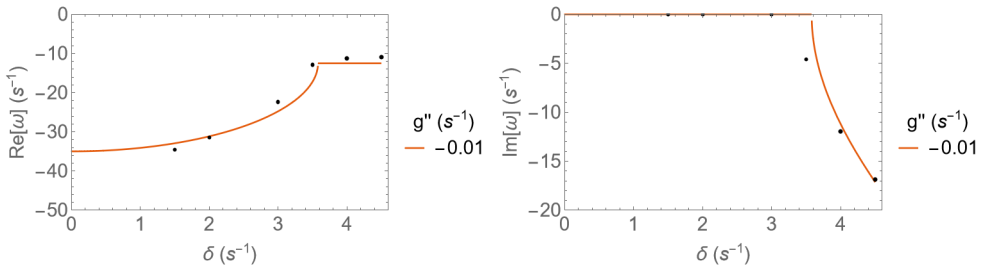

FIGURE B.2: The a) real and b) real components of the Bogoliobov frequency (denoted as Ω in text, ω in figure), as a function of detuning. at various fluctuation strengths

observe a transition between over to under-damped at approximately $\delta = 3.5\ \mathrm{s}^{-1}$, as well as correct scaling.

Acknowledgements

This research would not have been possible, if not for the support I have been given by the people around me. I'm extremely grateful to my supervisor, *Peter van der Straten*. I learned a lot over the course of this year, you encouraged me to come with my own idea's and helped me when I was stuck or discouraged. Much of my work and understanding on the theoretical side is due to *Henk Stoof*. I enjoyed the discussions we had together with Peter, it made made feel like we were pushing our understanding forward. I am also thankful to *Nejc Blaznik*, who helped me get acquainted with the lab. Although I couldn't spend as much time in the lab as we had hoped, I enjoyed our struggles together. The first half of my project I had the company of two fellow master students, also working on BEC's. *Amber*, I enjoyed your rants about cats and plants. And *Sam*, thanks for all the fun over these years. Major thanks to the *Nanophotonics Group* in general, our shared lunches and discussions were fun. The omnipresence of the infamous list made for some interesting social acrobatics. Outside of the university I could always count on my *family* to provide a listening ear, and a warm meal at times. Thanks for believing in me. As a trainer and vice president of Uboulder in addition to my academical work, I had my hands quite full at times. I like to extend my gratitude to my friends, for their understanding and support.

Bibliography

[1] M. Planck, "On the theory of the energy distribution law of the normal spectrum," *Dtsch. phys. Ges*, p. 237, 1900.

[2] Bose, "Plancks gesetz und lichtquantenhypothese," *Zeitschrift für Physik*, vol. 26, pp. 178–181, 1924. DOI: 10.1007/BF01327326.

[3] A. Einstein, "Quantentheorie des einatomigen idealen gases," *Sitzungsberichte der Preußischen Akademie der Wissenschaften*, pp. 245–257, 1924. DOI: https://doi.org/10.1002/3527608958.ch27.

[4] P. Kapitza, "Viscosity of liquid helium below the λ-point," *Nature*, 1938. DOI: 10.1038//141074a0.

[5] M. H. Anderson, J. R. Ensher, M. R. Matthews, C. E. Wieman, and E. A. Cornell, "Observation of bose-einstein condensation in a dilute atomic vapor," *Science*, vol. 269, no. 5221, pp. 198–201, 1995. DOI: 10.1126/science.269.5221.198.

[6] K. B. Davis, M. .-. Mewes, M. R. Andrews, *et al.*, "Bose-einstein condensation in a gas of sodium atoms," *Phys. Rev. Lett.*, vol. 75, pp. 3969–3973, 22 Nov. 1995. DOI: 10.1103/PhysRevLett.75.3969.

[7] E. Ooijen van, "Realization and illumination of bose-condensed sodium atoms," Ph.D. dissertation, May 2005.

[8] A. Groot, "Excitations in hydrodynamic ultra-cold bose gases," *PhD thesis*, Jun. 2015.

[9] J. Smits, "Space-time crystals in bose-einstein condensates," *PhD thesis*, Jul. 2021.

[10] E. Noether, "Invariante variationsprobleme," *Nachrichten von der Gesellschaft der Wissenschaften zu Göttingen, Mathematisch-Physikalische Klasse*, vol. 1918, pp. 235–257, 1918.

[11] F. Wilczek, "Quantum time crystals," *Physical Review Letters*, vol. 109, no. 16, Oct. 2012. DOI: 10.1103/physrevlett.109.160401.

[12] H. Watanabe and M. Oshikawa, "Absence of quantum time crystals," *Physical Review Letters*, vol. 114, no. 25, Jun. 2015. DOI: 10.1103/physrevlett.114.251603.

[13] V. K. Kozin and O. Kyriienko, "Quantum time crystals from hamiltonians with long-range interactions," *Phys. Rev. Lett.*, vol. 123, p. 210 602, 21 Nov. 2019. DOI: 10.1103/PhysRevLett.123.210602.

[14] A. Syrwid, J. Zakrzewski, and K. Sacha, "Time crystal behavior of excited eigenstates," *Phys. Rev. Lett.*, vol. 119, p. 250 602, 25 Dec. 2017. DOI: 10.1103/PhysRevLett.119.250602.

[15] B. Buča, J. Tindall, and D. Jaksch, "Non-stationary coherent quantum many-body dynamics through dissipation," *Nature Communications*, vol. 10, no. 1, Apr. 2019. DOI: 10.1038/s41467-019-09757-y.

[16] S. Choi, J. Choi, R. Landig, *et al.*, "Observation of discrete time-crystalline order in a disordered dipolar many-body system," *Nature*, vol. 543, Oct. 2016. DOI: 10.1038/nature21426.

[17] J. Zhang, P. Hess, A. Kyprianidis, *et al.*, "Observation of a discrete time crystal," *Nature*, vol. 543, Sep. 2016. DOI: 10.1038/nature21413.

[18] X. Yang and Z. Cai, "Dynamical transitions and critical behavior between discrete time crystal phases," *Physical review letters*, vol. 126, p. 020 602, Jan. 2021. DOI: 10.1103/PhysRevLett.126.020602.

[19] H. Keßler, P. Kongkhambut, C. Georges, L. Mathey, J. G. Cosme, and A. Hemmerich, "Observation of a dissipative time crystal," *Physical Review Letters*, vol. 127, no. 4, Jul. 2021. DOI: 10.1103/physrevlett.127.043602.

[20] J. N. Stehouwer, H. T. C. Stoof, J. Smits, and P. van der Straten, "Dynamics of spontaneous symmetry breaking in a space-time crystal," *Physical Review A*, vol. 104, no. 4, Oct. 2021. DOI: 10.1103/physreva.104.043324.

[21] C. J. Pethick and H. Smith, *Bose–Einstein Condensation in Dilute Gases*, 2nd ed. Cambridge University Press, 2008. DOI: 10.1017/CBO9780511802850.

[22] R. Corgier, "Engineered atomic states for precision interferometry," Ph.D. dissertation, Jul. 2019.

[23] S. Borman, *Crystallized time in ultra-cold bose gases*, Feb. 2022.

[24] L. Liao, J. Smits, P. van der Straten, and H. T. C. Stoof, "Dynamics of a space-time crystal in an atomic bose-einstein condensate," *Physical Review A*, vol. 99, no. 1, Jan. 2019. DOI: 10.1103/physreva.99.013625.

[25] J. Smits, L. Liao, H. T. C. Stoof, and P. van der Straten, "Observation of a space-time crystal in a superfluid quantum gas," *Phys. Rev. Lett.*, vol. 121, p. 185 301, 18 Oct. 2018. DOI: 10.1103/PhysRevLett.121.185301.

[26] J. Smits, H. Stoof, and P. van der Straten, "On the long-term stability of space-time crystals," *New Journal of Physics*, vol. 22, p. 105 001, Oct. 2020. DOI: 10.1088/1367-2630/abbae9.

[27] G. Fasshauer. "Runge-kutta methods." (), [Online]. Available: http://www.math.iit.edu/~fass/478578_Chapter_3.pdf (visited on 09/22/2022).

[28] B. Schmiedel. "Operating principle rk4." (2019), [Online]. Available: https://lowebms.readthedocs.io/en/latest/code/rk4.html (visited on 09/22/2022).

[29] J. Smits, H. T. C. Stoof, and P. van der Straten, "Spontaneous breaking of a discrete time-translation symmetry," *Physical Review A*, vol. 104, no. 2, Aug. 2021. DOI: 10.1103/physreva.104.023318.

[30] D. Steck, *Sodium d line data*, Jan. 2009.

[31] W. Ketterle, D. S. Durfee, and D. M. Stamper-Kurn, "Making, probing and understanding bose-einstein condensates," 1999. DOI: 10.48550/ARXIV.COND-MAT/9904034.

[32] S. Loth, *Holographic imaging of bose-einstein condensates*, Jun. 2018.

[33] J. W. Goodman, *Introduction to Fourier optics*. 2005, vol. 1.

[34] T. Zibold, E. Nicklas, C. Gross, and M. K. Oberthaler, "Classical bifurcation at the transition from rabi to josephson dynamics," *Physical Review Letters*, vol. 105, no. 20, Nov. 2010. DOI: 10.1103/physrevlett.105.204101.

[35] Z. R. Lin, Y. Nakamura, and M. I. Dykman, "Critical fluctuations and the rates of interstate switching near the excitation threshold of a quantum parametric oscillator," *Physical Review E*, vol. 92, no. 2, Aug. 2015. DOI: 10.1103/physreve.92.022105.

[36] R. Gati and M. K. Oberthaler, "A bosonic josephson junction," *Journal of Physics B: Atomic, Molecular and Optical Physics*, vol. 40, no. 10, R61–R89, May 2007. DOI: 10.1088/0953-4075/40/10/r01.

[37] O. Chuikin, Y. Greenberg, and A. Shtygashev, "Damping of vacuum rabi oscillations in a two-qubit structure in a high-q cavity," *Physics of the Solid State*, vol. 62, pp. 1571–1579, Sep. 2020. DOI: 10.1134/S106378342009005X.

[38] R. Khasseh, A. Russomanno, and R. Fazio, "Fragility of classical hamiltonian period doubling to quantum fluctuations," *Physical Review B*, vol. 104, no. 13, Oct. 2021. DOI: 10.1103/physrevb.104.134309.

[39] Y. Pan and B. Wang, "Time-crystalline phases and period-doubling oscillations in one-dimensional floquet topological insulators," *Physical Review Research*, vol. 2, Nov. 2020. DOI: 10.1103/PhysRevResearch.2.043239.